J. Fluid Mech. (2021), *vol*. 908, A28. © The Author(s), 2020.
Published by Cambridge University Press
doi:10.1017/jfm.2020.869

Heat transfer in a turbulent channel flow with super-hydrophobic or liquid-infused walls

Umberto Ciri[1] **and Stefano Leonardi**[1],†

[1]Department of Mechanical Engineering, The University of Texas at Dallas, Richardson, TX 75080, USA

(Received 30 January 2020; revised 2 September 2020; accepted 11 October 2020)

Heat transport over super-hydrophobic (SHS) and liquid-infused surfaces (LIS) is studied using direct numerical simulations of a turbulent channel flow. The lower wall of the channel consists of either longitudinal or transversal bars with a secondary fluid locked in the cavities between the surface elements. We consider two viscosity ratios between the fluids mimicking SHS and LIS. The thermal diffusivity is varied to assess its effect on thermal performance. We investigate the dependence of heat transfer on the elements pitch-to-height ratio and on the interface dynamics. The interface deformation (dependent upon the surface tension between the two fluids) is fully coupled to the fluid governing equations with the level-set method. Present simulations are consistent with published results about the drag-reducing potential of SHS and LIS in turbulent flow compared to the smooth wall. In the limiting case of infinite surface tension (the interface remains flat and slippery), heat transfer efficiency (heat transfer to drag ratio) can be enhanced compared to a smooth wall. Although the total heat flux is marginally reduced, SHS and LIS with longitudinal ridges achieve a comparatively larger drag reduction, which increases the efficiency. A model is derived from the energy equation to correlate the heat transfer performance with the thermal slip length (b_θ), analogous to the streamwise slip length (b) used in the literature to scale drag reduction. Consistently with the model, results show that heat transfer efficiency is larger than for a smooth wall when the thermal slip length is smaller than the streamwise slip length (longitudinal bars). Vice versa, transversal bars present $b/b_\theta < 1$ and a smaller heat transfer efficiency than the smooth wall. In the case of finite surface tension, the dynamics of the interface generates a turbulent flux which improves the thermal performance, but tends to decrease the amount of drag reduction. Liquid-infused surfaces are more robust than SHS to the deformation of the interface thanks to the larger viscosity of the secondary fluid and maintain about the same drag reduction as in the infinite surface tension case. For SHS longitudinal bars, simultaneous increase in heat transfer and reduction in drag are observed, leading to an apparent breakdown of the Reynolds analogy. Also in the case of finite surface tension, heat transfer efficiency scales with the relative magnitude of the thermal and streamwise slip lengths. The results suggest a potential expansion of the control space for engineers. Depending on the application, one can reach an optimal combination of heat transfer and drag by tuning the shape of the substrate and the viscosity and diffusivity ratios.

Key words: turbulence simulation, drag reduction, mixing enhancement

† Email address for correspondence: stefano.leonardi@utdallas.edu

1. Introduction

The transport of heat and momentum in turbulent flows is common in many engineering applications. Turbulent motion may either promote or hamper the achievement of the desired system performance. For instance, the increased friction drag compared to laminar flow conditions increases costs for marine, terrestrial or aerial vehicles. On the other hand, turbulence is beneficial in cooling systems and heat exchangers because of the enhanced fluid particle mixing.

For this reason, methods to promote and exploit turbulent motion are employed in thermal applications. Rough walls are widely used to increase the turbulence intensity and enhance heat transfer. For instance, the internal ducts of gas turbine blades present rib turbulators or pin fins to increase recirculation and mixing (Han, Dutta & Ekkad 2000; Sewall *et al.* 2006). Many efforts have been devoted to optimize the rib design parameters, including shape, pitch-to-height ratio, height of the turbulator and inclination with respect to the mean stream (Han, Zhang & Lee 1991; Han & Zhang 1992; Ekkad & Han 1997; Ekkad, Huang & Han 1998; Tanda 2004; Won & Ligrani 2004; Tachie *et al.* 2009). Large heat transfer coefficients are obtained because of strong streamwise vortices generated by the ribs in the channel (Hetsroni *et al.* 1999; Miyake, Tsujimoto & Nakaji 2001; Leonardi *et al.* 2004). The increase in heat transfer rate compared to the smooth wall due to roughness is notable. Direct numerical simulations (DNS) of turbulent flow over periodic roughness elements performed by Leonardi *et al.* (2015) show that the heat flux may be as twice as large depending on the pitch-to-height ratio of the elements. However, the heat transfer augmentation is also accompanied by a drag increase (Promvonge & Thianpong 2008; Leonardi *et al.* 2015). In most cases, this is related to the additional form drag associated with the geometry of the roughness elements (Leonardi *et al.* 2003; Leonardi & Castro 2010).

Efforts to combine heat transfer enhancement with simultaneous drag reduction have been elusive. Longitudinal grooves (or 'riblets') of various cross-sectional shape have been proposed as a passive mean of drag reduction, based on the observation that shark skin presents a similar morphology (Walsh 1982, 1983). Experimental and numerical assessments have shown turbulent drag reduction compared to a smooth wall of the order of 5–10 % (Bechert, Hoppe & Reif 1985; Choi, Moin & Kim 1993) depending on the riblets size in wall units. Early experimental results (Lindemann 1985; Choi & Orchard 1997) also suggested that the heat transfer rate could be increased with riblets. However, recent DNS (Stalio & Nobile 2003; Orlandi, Sassun & Leonardi 2016) report an opposite behaviour, observing heat transfer reduction in the riblets drag-reducing regime and Prandtl number dependence.

Recently, two novel passive methods have been proposed for turbulent drag reduction, which combine textured micro-structures with a secondary fluid trapped in the cavities. In super-hydrophobic surfaces (SHS) the surface structures (micro-posts or micro-ridges) have a thin-film hydrophobic coating, which traps air in the cavities when the surface is submerged in water. Liquid-infused surfaces (LIS) are conceptually similar, although an oil lubricant is typically used instead of air as the secondary fluid. The oil remains locked in the substrate cavities thanks to the micro-nanostructure.

The mechanism of drag reduction is similar in both cases. The presence of pockets filled with secondary fluid creates a heterogeneous boundary with fluid-fluid and solid-fluid interfaces. The overall effect is to create an average 'slip' velocity U_s over the surface. The slip velocity is associated to a slip length, defined as the distance from the interface of the virtual origin of the velocity profile extrapolated with the gradient at the interface. The slip length is analogous to the 'protrusion height', which is the parameter commonly referred

to when analysing the performance of riblets (Luchini, Manzo & Pozzi 1991; Rastegari & Akhavan 2018). The drag reduction is correlated with the slip velocity and the slip length, with higher values providing a larger amount of drag reduction (Park, Park & Kim 2013; Rastegari & Akhavan 2015; Chang *et al.* 2019).

Experimental and numerical investigations have shown promising results for LIS and SHS to reduce drag (Daniello, Waterhouse & Rothstein 2009; Martell, Perot & Rothstein 2009; Park *et al.* 2013; Rosenberg *et al.* 2016; Seo & Mani 2016; Fu *et al.* 2017; Van Buren & Smits 2017), at least if the two-fluid interface remains flat (García Cartagena *et al.* 2018). Heat transfer over these surfaces has not received as much attention. Previous studies in the literature have considered heat transfer in super-hydrophobic micro-channels under laminar flow conditions, which are of interest for cooling in micro-electronic applications (Kirk, Hodes & Papageorgiou 2017). Maynes, Webb & Davies (2008) carried out two-dimensional simulations of a micro-channel with super-hydrophobic transversal grooves with a flat interface. The local Nusselt number over the solid ribs is increased compared to the smooth wall. However, the total heat flux (i.e. including the heat flux contributions over the cavities) reduces because of the high thermal resistance of the air pocket. Rosengarten, Stanley & Kwok (2007) found similar results suggesting SHS micro-channels to be used as insulators in micro-devices with a high-temperature working fluid. Other studies (Maynes *et al.* 2013; Enright *et al.* 2014; Maynes & Crockett 2014; Ng & Wang 2014) have investigated the dependence upon the substrate texture of the heat transfer rate and the so-called temperature jump length or thermal slip length. The thermal slip length is the analogous for temperature (and heat flux) to the streamwise slip length used to scale drag reduction for both LIS and SHS (Rastegari & Akhavan 2015; Fu *et al.* 2017). Assuming Stokes' or creeping motion, these studies have found the thermal slip length to increase (hence, the temperature gradient, and the heat flux, to decrease) with the texture gas fraction, which is consistent with the simulations by Maynes *et al.* (2008). In general, the non-dimensional heat flux or Nusselt number are reduced in super-hydrophobic laminar micro-channels. However, the concurrent drag reduction provided by the slip at the interface allows for an increased flow rate for a fixed pressure drop across the channel, which could amount to an improved global heat transfer capacity (Cheng, Xu & Sui 2015; Lam, Hodes & Enright 2015).

Previous studies have focused on the laminar flow over SHS, while less is known on the turbulent regime. This paper aims at filling this gap by discussing direct numerical simulation results of turbulent flow and heat transfer over LIS and SHS. Studying the thermal performance of these surfaces in turbulent flows is motivated by the inherent enhanced mixing capacity compared to laminar flows. Direct numerical simulations of a channel flow with two superposed fluids and a textured wall are performed. The viscosity ratio between the two fluids is varied to reproduce characteristic values for SHS and LIS, while at first uniform thermal conductivity is assumed to emphasize the role of turbulent flow in the heat transfer process. Subsequently, a parametric study on the effect of the fluids' thermal properties is performed.

The remainder of this paper is organized as follows. First, the numerical method and the simulation set-up are described in § 2. Then, results are presented for a set of simulations in which the interface between the fluids is assumed to remain flat and slippery (§ 3). The effect of the interface dynamics is discussed in § 4. Section 5 contains the analysis on the sensitivity to the fluid properties. Concluding remarks are presented in § 6.

2. Numerical method

Direct numerical simulations of two overlying immiscible fluids in a channel with a textured wall have been performed. The governing equations are the (non-dimensional)

continuity, Navier–Stokes and energy equations:

$$\frac{\partial U_i}{\partial x_i} = 0, \tag{2.1}$$

$$\frac{\partial U_i}{\partial t} + \frac{\partial}{\partial x_j}\left(U_i U_j\right) = -\frac{\partial P}{\partial x_i} + \Pi\delta_{i1} + \frac{1}{Re}\frac{\partial}{\partial x_j}\left[\tilde{\mu}\left(\Phi\right)\left(\frac{\partial U_i}{\partial x_j} + \frac{\partial U_j}{\partial x_i}\right)\right] + f_i, \tag{2.2}$$

$$\frac{\partial T}{\partial t} + \frac{\partial}{\partial x_j}\left(T U_j\right) = \frac{1}{RePr}\frac{\partial}{\partial x_j}\left[\tilde{\alpha}\left(\Phi\right)\frac{\partial T}{\partial x_j}\right]. \tag{2.3}$$

Here U_i is the component of the velocity vector in direction x_i, P is the pressure and T the fluid temperature; Π is the pressure gradient required to maintain a constant flow rate in the channel and δ_{ij} is the Kronecker's delta. The external pressure gradient is applied to the primary fluid as well as to the secondary fluid, which is thus driven by both the forcing Π and the shear of the overlying fluid.

The Reynolds number is based on the channel half-height h, the (constant) bulk velocity U_b and the viscosity of the overlying fluid (ν_2). For the present simulations, $Re = U_b h/\nu_2 = 2800$, which for a canonical channel corresponds to $Re_\tau = u_\tau h/\nu_2 = 180$ (where u_τ is the friction velocity). The Prandtl number, $Pr = \nu_2/\alpha_2$, is also defined with the properties of the fluid in the bulk channel, with α_2 being the thermal diffusivity.

The marker functions $\tilde{\mu}(\Phi)$ and $\tilde{\alpha}(\Phi)$ discriminate between the properties of the two fluids based on the signed distance from the interface Φ. Here Φ is taken as positive above the interface, and negative below. The two functions are defined as

$$\tilde{\mu}\left(\Phi\right) = m + (1-m)\,H\left(\Phi\right), \tag{2.4}$$

$$\tilde{\alpha}\left(\Phi\right) = a + (1-a)\,H\left(\Phi\right), \tag{2.5}$$

where $m = \mu_1/\mu_2$ and $a = \alpha_1/\alpha_2$ are the viscosity and diffusivity ratios between the fluids, respectively. Here H is the Heaviside function ($H = 1$ if $\Phi > 0$, main fluid, and $H = 0$ if $\Phi < 0$, secondary fluid). Two different viscosity ratios have been considered: $m = \mu_1/\mu_2 = 0.01$, characteristic of SHS (water over air), and $m = 0.4$, typical for LIS (water over heptane). The thermal diffusivity ratio, $a = \alpha_1/\alpha_2$, is initially taken as unity. This value as well as the unitary Prandtl number ($Pr = 1$) have been chosen to isolate the effect of turbulent motion on heat transfer. Subsequently, a parametric study on the fluids' thermal properties has been performed using values for Pr and a representative of LIS and SHS. We remark that this study does not attempt to reproduce a particular combination of fluids in SHS or LIS. We vary m and a, while keeping the density ratio unity, to isolate the effect of viscosity and thermal diffusivity on the heat transfer. We also assume that the interface remains pinned to the textures.

The body force f_i in (2.2) accounts for the interface between the fluids through the continuous surface force method (Brackbill, Kothe & Zemach 1992; Chang *et al.* 1996). The interfacial force depends on the surface tension, σ, and the geometry of the interface:

$$f_i = \frac{1}{We}\kappa n_i \delta(\Phi). \tag{2.6}$$

Here $We = \rho U_b^2 h/\sigma$ is the Weber number, κ is the curvature of the interface and n_i is the component of the normal to the interface in direction x_i; $\delta(\Phi)$ indicates the Dirac delta function. The interface is initially at the crest plane, and the secondary fluid fills the cavities in the substrate. To study the effect of the deformation of the interface on the heat transfer, we consider two values of the Weber number: (i) $We = 0$, corresponding to

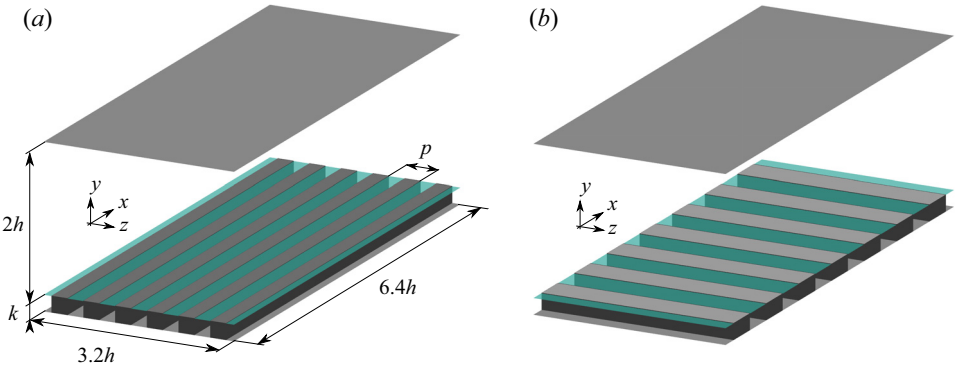

FIGURE 1. Channel configuration: (*a*) longitudinal bars; (*b*) transversal bars. The turquoise surface at the crest plane is the interface.

the asymptotic limit of infinite surface tension; and (ii) $We = 40$, which approximately corresponds to a capillary number $Ca = We^+ = \mu_2 u_\tau/\sigma \sim 10^{-3}$. In the first case (infinite surface tension), the interface remains flat and slippery in the in-plane directions. The force f_i is directed along the wall-normal direction (x_2 or y) and computed such that the normal velocity is zero at the interface location. In the second case ($We^+ = 10^{-3}$), the interface is deformable and its position is tracked with the level-set method (Sethian & Smereka 2003). That is, the signed distance function Φ evolves according to

$$\frac{\partial \Phi}{\partial t} + \frac{\partial}{\partial x_j}\left(\Phi U_j\right) = 0, \tag{2.7}$$

where Φ is the signed distance function and U_j is the velocity field. Thus, the interface dynamics is fully coupled with the Navier–Stokes equations. The force f_i is computed with (2.6) and is perpendicular to the interface.

The numerical solution of (2.1)–(2.3) is discussed in detail in Orlandi (2000). The staggered central second-order finite-difference scheme is used to discretize the spatial derivatives in an orthogonal coordinate system. A fractional step method, with linear terms treated implicitly and convective terms treated explicitly, is used to advance the equation in time. The matrix resulting from the implicit terms is inverted with an approximate factorization technique. The momentum equations are advanced with the pressure at the previous step, yielding an intermediate non-solenoidal velocity field. A scalar quantity is used to project the non-solenoidal field onto a solenoidal one. A hybrid low-storage third-order Runge–Kutta scheme is used to advance the equations in time. The substrate textures are treated with the immersed boundary method described in detail in Orlandi & Leonardi (2006). The numerical implementation of the level-set method (2.7) is detailed in García Cartagena *et al.* (2018).

Simulations are performed for a turbulent channel flow with texture on the lower wall (figure 1). The surface textures consist of either longitudinal or transversal bars. The height of the ridges is $k = 0.05h$. Three values for pitch p between two consecutive ridges are considered, specifically $p/k = 2, 4, 8$. The gas fraction (i.e. the ratio of the volume of the cavities to the total volume in the substrate) is kept constant for the different pitch values and equal to 50 %. The computational box is $6.4h \times 2.05h \times 3.2h$ in the streamwise (x), wall-normal (y) and spanwise (z) directions, respectively. The additional $0.05h$ increase in channel height corresponds to the cavity height where the surface textures are placed.

Details on the grid resolution are discussed in the appendix. Periodic boundary conditions are applied in the streamwise and spanwise directions. No-slip conditions are imposed on the channel walls. Isothermal boundary conditions are applied on the two walls, with the textured wall at temperature T_w^* and the upper wall at $T_u^* < T_w^*$ ('$*$' denotes dimensional quantities). The temperature in (2.3), and in the remainder of the paper, is normalized as $T = 1 - 2[(T^* - T_w^*)/(T_u^* - T_w^*)]$. Thus, it is equal to $T = 1$ on the textured wall, and equal to $T = -1$ on the upper smooth wall. The flow field is initialized with a parabolic velocity profile in the streamwise direction above the crest plane. Disturbances are applied to promote transition to turbulence. The initial temperature profile varies linearly from $T = T_w = 1$ at the crest plane to $T = T_u = -1$ at the top wall. In the substrate the temperature is initially uniform at $T = T_w$, and the velocity is zero. No disturbances are applied to the secondary flow in the textures.

3. Surface performance in ideal conditions: flat interface

The results for the idealised case of infinite surface tension ($We = 0$) are presented first. In LIS and SHS the secondary fluid and the substrate texture create heterogeneous solid-fluid and fluid-fluid interfaces at the crest plane. Over the fluid-fluid interface (above the cavities) the primary stream can slip. From a macroscopic point of view, this generates a non-zero 'effective' slip length b, defined as

$$\bar{U}_s = b \left. \frac{\mathrm{d}\bar{U}}{\mathrm{d}y} \right|_{y_w}, \tag{3.1}$$

where $\bar{U}_s$ is the apparent 'slip' velocity at the crest plane (Lauga, Brenner & Stone 2007); y_w indicates the crest plane and $\mathrm{d}\bar{U}/\mathrm{d}y$ is the local gradient in the normal direction. The overline denotes an average in time and in the streamwise and spanwise directions. Thus, the slip length is the distance from the crest plane, where the extrapolated velocity profile vanishes. The slip conditions at the interface affect the performance of LIS and SHS, in particular the drag reduction DR, defined as

$$DR = \frac{\tau_0 - \tau}{\tau_0}, \tag{3.2}$$

where τ indicates the surface drag and subscript '0' refers to the smooth wall benchmark. The correlation between the amount of drag reduction and the slip length has been widely reported in the literature (Fukagata, Kasagi & Koumoutsakos 2006; Park *et al.* 2013; Jung, Choi & Kim 2016; Seo & Mani 2016; Fu *et al.* 2017; García Cartagena *et al.* 2018; Rastegari & Akhavan 2015, 2018; Arenas *et al.* 2019; Chang *et al.* 2019). Present results, compiled in table 1 and shown in figure 2, corroborate to a large extent this observation. In figure 2 the DR is plotted as a function of the slip length in 'nominal' wall units, $b^{+0} = bu_{\tau,0}/\nu$ (where $u_{\tau,0} = \sqrt{\tau_0/\rho}$ is the friction velocity of the reference smooth channel). This is done consistently with the analytical model derived by Rastegari & Akhavan (2015) (also shown in the figure):

$$DR = \frac{b^{+0}}{b^{+0} + Re/Re_{\tau,0}} + \tilde{g}\,(\varepsilon)\,. \tag{3.3}$$

Here $\tilde{g}(\varepsilon)$ accounts for the effect of the modification of turbulent structures and secondary motion on drag. Longitudinal bars show a very good agreement with the 'slip' term in (3.3) for $b^{+0} \lesssim 5$. For larger values of the slip length, that is, for larger p/k, secondary

Texture	m	p/k	Re_τ	DR (%)	HTE (%)	q/τ	b^+	b_θ^+
Longitudinal	0.01	2	171.4	+9.1	−3.8	1.06	1.74	0.67
Longitudinal	0.01	4	164.8	+15.9	−5.9	1.12	3.02	1.27
Longitudinal	0.01	8	162.4	+18.3	−6.3	1.15	4.74	2.05
Longitudinal	0.4	2	173.5	+6.8	−4.0	1.03	1.15	0.68
Longitudinal	0.4	4	167.9	+12.7	−6.7	1.07	2.07	1.27
Longitudinal	0.4	8	162.3	+18.4	−7.9	1.13	3.30	2.00
Transversal	0.01	2	183.7	−4.4	−3.7	0.92	0.62	1.14
Transversal	0.01	4	183.0	−3.6	−4.3	0.92	0.96	1.67
Transversal	0.4	2	183.2	−3.9	−1.4	0.95	0.43	1.02
Transversal	0.4	4	182.3	−2.9	−1.6	0.96	0.67	1.50

TABLE 1. Summary of surface performances for $We = 0$. The drag reduction is $DR = 1 - \tau/\tau_0$, where τ is the drag of the textured wall (one wall only), τ_0 is the friction for a smooth channel; the heat transfer enhancement is defined as $HTE = q/q_0 - 1$, where q is the heat flux at the textured surface (q_0 is the equivalent value for the smooth channel); $b^+ = bu_\tau/\nu$ and b_θ^+ are the slip lengths in wall units.

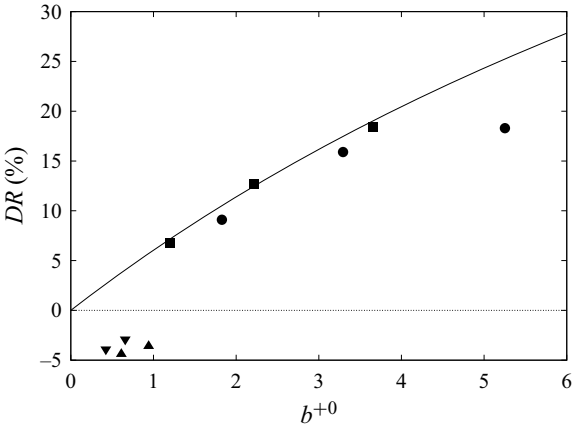

FIGURE 2. Drag reduction for the $We = 0$ case as a function of the slip length in 'nominal' wall units. Symbols, present simulations: longitudinal bars, $m = 0.01$ • and $m = 0.4$ ■; transversal bars, $m = 0.01$ ▲ and $m = 0.4$ ▼. Lines: (3.3) with $\tilde{g} \equiv 0$.

motion in the channel becomes more intense and the amount of drag reduction decreases with respect to the theoretical limit (3.3 with $\tilde{g} \equiv 0$). Transversal textures have a small slip length ($b^+ < 1$) and are drag increasing ($DR < 0$) with respect to the smooth wall.

Analogously to the momentum slip length, the thermal slip length b_θ can be defined as

$$T_w - \bar{T}_s = -b_\theta \left.\frac{\mathrm{d}\bar{T}}{\mathrm{d}y}\right|_{y_w}, \tag{3.4}$$

where $\bar{T}_s = \bar{T}(y_w)$ is the average temperature at the crest plane. Thus, the thermal slip length is the distance from the crest plane at which the extrapolated temperature profile reaches the 'no-slip' isothermal value T_w. In analogy with the drag case, a larger b_θ is expected to be associated with a reduced heat transfer rate, because of

the consequent reduced temperature gradient. The relationship between b_θ and the heat transfer performance can be analytically derived from the energy equation. Following an analogous procedure to Fukagata, Iwamoto & Kasagi (2002), after averaging in time and in the horizontal directions (i.e. in x and z directions), the dimensional form of (2.3) reduces to

$$\frac{\partial}{\partial y}\left[-\alpha(y)\frac{\partial \bar{T}}{\partial y}+\overline{\theta v}\right]=0. \tag{3.5}$$

The overline denotes the average, $\overline{\theta v}$ are the convective fluxes along the wall-normal direction ($\theta = T(x, y, z, t) - \bar{T}(y)$ and $v = V(x, y, z, t) - \bar{V}(y)$, with $\bar{V}(y) = 0$ for continuity), which consist of both the dispersive component (due to texture periodicity) and the turbulent component. Equation (3.5) implies that the total heat flux is constant throughout the channel height. In the case of a flat and slippery interface, where $V = 0$, its value, q, is equal to the molecular heat flux at the interface, $y = 0$. Therefore, after integrating from the crest plane ($y = 0$, which is also the interface position) to a generic y in the primary fluid domain:

$$-\alpha_2\frac{\partial \bar{T}}{\partial y}+\overline{\theta v}=\frac{q}{\rho c_p}. \tag{3.6}$$

Here ρ is density and c_p the specific heat. Integration from the crest plane ($y = y_w$, or $y = 0$ in the present reference frame) to the top wall ($y = 2h$) yields

$$\alpha_2\left(\bar{T}_s-T_u\right)+\int_0^{2h}\overline{\theta v}\,\mathrm{d}y=\frac{q}{\rho c_p}2h, \tag{3.7}$$

where $\bar{T}_s$ is the average temperature at the interface (analogous to the slip velocity) and T_u is the temperature of the upper wall, which is constant because of the isothermal boundary condition. Normalizing the fluxes inside the integral in wall units and using the change of variable $\eta = y/h$, we have

$$\alpha_2\left(\bar{T}_s-T_u\right)+h\frac{q}{\rho c_p}\int_0^2\overline{\theta^+v^+}\,\mathrm{d}\eta=\frac{q}{\rho c_p}2h. \tag{3.8}$$

Here, $\overline{\theta^+v^+}=\overline{\theta v}\rho c_p/q=\overline{\theta v}/(T_\tau u_\tau)$, where $T_\tau = q/\rho c_p u_\tau$ is the 'friction' temperature. Introducing the Stanton number, $St = q/\rho c_p U_b(T_w - T_u)$, (3.8) reads as

$$\frac{1}{RePr}\left(\frac{\bar{T}_s-T_u}{T_w-T_u}\right)+St\int_0^2\overline{\theta^+v^+}\,\mathrm{d}\eta=2St, \tag{3.9}$$

which can be recast as

$$St=\frac{1}{RePr}\left(1-\frac{T_w-\bar{T}_s}{T_w-T_u}\right)\frac{1}{2-I^+} \tag{3.10}$$

with $I^+ = \int_0^2 \overline{\theta^+v^+}\,\mathrm{d}\eta$. From the energy balance (3.6) in wall units, it follows that $0 < I^+ < 2$, so that the denominator in (3.10) is positive and does not vanish. Using (3.10),

the heat transfer enhancement with respect to a smooth wall ($HTE = St/St_0 - 1$) can be expressed as

$$HTE = -\frac{T_w - \bar{T}_s}{T_w - T_u} + \left(1 + \frac{T_w - \bar{T}_s}{T_w - T_u}\right)\frac{\varepsilon}{2 - I^+},$$
$$= -\frac{T_w - \bar{T}_s}{T_w - T_u} + g_\theta(\varepsilon), \tag{3.11}$$

where $\varepsilon = I^+ - I_0^+$ is the difference in the convective fluxes between the textured surface and the smooth wall. From (3.11), the change in heat transfer can be attributed either to heterogeneity of the temperature distribution at the crest plane (for which $\bar{T}_s \neq T_w$) or to the convection in the overlying fluid. In general, since $\bar{T}_s < T_w$, an increase in heat transfer can be expected only if turbulent convection (that is, the g_θ contribution) is enhanced.

Equation (3.11) is analogous to the relationship derived by Rastegari & Akhavan (2015) for the drag reduction,

$$DR = \frac{\bar{U}_s}{U_b} + g(\varepsilon), \tag{3.12}$$

where $g(\varepsilon)$ is a function that accounts for the difference in the Reynolds stresses $\overline{uv}$ between the textured surface and the smooth wall and has a similar structure to g_θ in (3.11) (see (2.5) of Rastegari & Akhavan 2015). By introducing the slip length b, (3.12) can be expressed in the form of (3.3). Similarly, using the thermal slip length of (3.4), the Reynolds analogy ($St_0 = C_{f,0}/2 = Re_{\tau,0}^2/Re^2$, where $C_{f,0} = \tau_0/\frac{1}{2}\rho U_b^2$ is the friction coefficient, Kestin & Richardson (1963)) and the identities

$$T_s^+ = b_\theta^+ Pr, \tag{3.13}$$

$$\frac{T_w - \bar{T}_s}{T_w - T_u} = b_\theta^{+0}\,(HTE + 1)\,\frac{Re_{\tau,0}}{Re}Pr, \tag{3.14}$$

(3.11) can be expressed as

$$HTE = -\frac{b_\theta^{+0} Pr}{b_\theta^{+0} Pr + Re/Re_{\tau,0}} + \tilde{g}_\theta(\varepsilon), \tag{3.15}$$

where $b_\theta^{+0} = b_\theta u_{\tau,0}/\nu$ is the nominal value of thermal slip length in wall units. Here $\tilde{g}_\theta$ accounts for the modifications in the convective fluxes compared to the smooth wall as in (3.11). Equation (3.15) is analogous to (3.3) for the drag reduction.

In figure 3 results from the simulations are compared against the analytical model in (3.15). Only the 'slip' contribution is considered in figure 3, i.e. $\tilde{g}_\theta \equiv 0$. In general, there is a relatively larger departure from the model trend compared to figure 2, especially as $b_\theta^{+0} > 1$. For larger values of the thermal slip lengths, modifications to turbulence and secondary motion becomes significant, which is expected as the textures are larger. This suggests that the thermal balance is more sensitive than momentum transport to the turbulent and secondary motions over the textures. Such different sensitivity can be traced back to the dissimilarity in the momentum and temperature governing equations and boundary conditions. The momentum balance integrated across the channel reads as

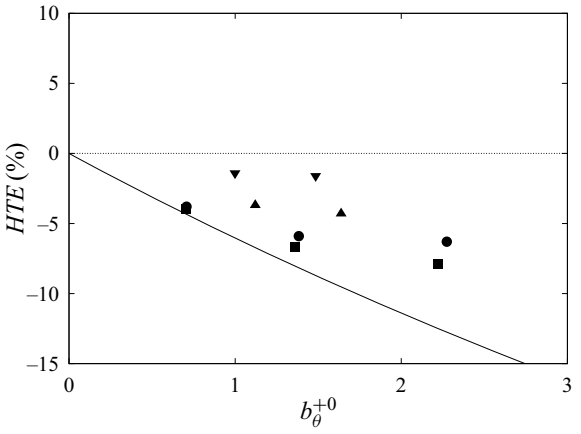

FIGURE 3. Heat transfer enhancement for the $We = 0$ as a function of the thermal slip lengths in 'nominal' wall units. Symbols, present simulations: longitudinal bars, $m = 0.01$ • and $m = 0.4$ ■; transversal bars, $m = 0.01$ ▲ and $m = 0.4$ ▼. Lines: (3.15) with $\tilde{g}_\theta \equiv 0$.

(Rastegari & Akhavan 2015):

$$\frac{6}{Re}\left(1 - \frac{\bar{U}_s}{U_b}\right) + 3C_f \int_0^1 \overline{u^+ v^+}\,(1-\eta)\,\mathrm{d}\eta = C_f. \tag{3.16}$$

The integrals of the fluxes $\overline{uv}$ and $\overline{\theta v}$ contribute to the terms $\tilde{g}$ and $\tilde{g}_\theta$ in the expressions for *DR* and *HTE*, respectively. However, as shown by (3.9) and (3.16), they are weighted by a different factor, dependent on the distance from the crest plane (i.e. $1 - \eta$ for $\overline{uv}$, 1 for $\overline{\theta v}$). Therefore, even in the presence of similar solutions for the turbulent fluctuations u and θ, a different sensitivity of *HTE* and *DR* to the secondary motion could be expected. The weighting factor depends on the channel configuration and the boundary conditions. For instance, Kasagi *et al.* (2012) have considered a channel with both smooth walls and different boundary conditions for the temperature field. Following a similar approach to derive (3.9), different weighting factors are obtained for the contribution of the turbulent heat flux to the Stanton number. They suggest this as a possible mean to achieve 'dissimilar control' (i.e. simultaneous heat transfer enhancement and drag reduction), and present an application using opposition control through blowing and suction. More in general, a dissimilarity in the change in thermal and momentum performance with respect to the smooth wall is also observed for flow over rough walls. In this case, the drag increases more than the heat transfer (see, e.g. Leonardi *et al.* 2015). Ultimately, the reason for the different behaviour is that the temperature is a scalar field, while the streamwise velocity is a component of a solenoidal vector field. A departure from similarity can be expected when pressure gradients become important in the flow (as, for example, for rough walls), since there is no counterpart for this mechanism in the energy balance for the temperature dynamics.

For a given pitch and texture orientation, SHS and LIS have similar heat transfer performance. The dependence on the surface type is probably mitigated by the assumption of uniform thermal diffusivity across the two fluids ($a = 1$). The residual discrepancy, which is larger for increasing pitch, is to ascribe to the turbulent motion over LIS and SHS. Transversal bars have a larger heat flux compared to longitudinal bars, which is expected since a larger heat flux generally corresponds to a larger drag. However, for all textures,

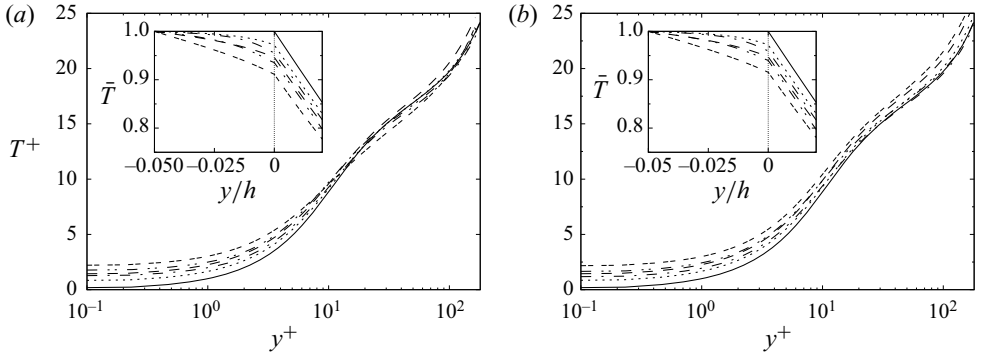

FIGURE 4. Mean temperature profile for SHS (*a*) and LIS (*b*): ——— smooth channel; ····· longitudinal ridges, $p/k = 2$; – – – – longitudinal ridges, $p/k = 4$; -- -- longitudinal ridges, $p/k = 8$; —·— transversal bars, $p/k = 2$; —··— transversal bars, $p/k = 4$.

the heat flux is reduced compared to the smooth wall ($HTE < 0$), although the magnitude of the decrease remains limited ($\lesssim 10\,\%$).

In the temperature profiles in figure 4, normalized in wall units $T^+ = (T_w - \bar{T})\rho c_p u_\tau / q$, an upward shift in the near-wall region is observed. The shift depends on the 'slip temperature' and the profiles in the sublayer collapse when plotted as $T^+ - T_s^+$, similarly to the velocity case with scaling $U^+ - U_s^+$ (Orlandi, Leonardi & Antonia 2008). From (3.11), the magnitude of the shift T_s^+ or, equivalently, its value in physical units, $T_w - \bar{T}_s$ (shown in the inset of figure 4), is a measure of the heat transfer reduction. For a given pitch and viscosity ratio, the shift is larger for transversal bars, even though this texture orientation has superior heat transfer performance than longitudinal ridges. This implies that fluxes $\overline{\theta v}$ compensate for the reduction in the temperature gradient to a larger extent. A notable increase in heat flux is observed in the near-wall region for transversal bars (figure 5). The normalization in wall units is a ratio of the convective heat flux to the total heat flux (Kim & Moin 1987). The near-wall peak contributes for more than 10 % of the surface heat flux in the case of SHS and slightly less than that for LIS. The enhanced heat flux is not due to changes in the structure of the overlying turbulent flow, but rather to the heterogeneity in the crest plane. Using the triple decomposition (Hussain & Reynolds 1970), one can separate the contributions to the total convective flux ($\overline{\theta v}$) of the random (turbulent) component and the dispersive component (Leonardi *et al.* 2015):

$$\overline{\theta v} = \theta v_{disp} + \overline{\theta' v'}. \tag{3.17}$$

Here $\theta' = T - \langle T \rangle$ and angle brackets denote the ensemble average of points at the same relative position within the periodic texture. The dispersive heat flux is $\theta v_{disp} = \overline{\tilde{\theta}\tilde{v}}$, where $\tilde{\theta} = \langle T \rangle - \bar{T}$ is the coherent fluctuation, due to the surface texture. As shown in the inset of figure 5, over the crest plane, the flux is mostly due to the dispersive component. The dispersive component is related to heterogeneity in the mean flow and is strongly affected by the texture geometry. In particular, the bar orientation seems a primary factor, with longitudinal bars not presenting a near-wall peak in the dispersive stress distribution. In the outer region the heat flux is carried by the turbulent component, but its distribution is not significantly modified compared to the smooth wall case. This is different than the classic case of rough walls. Leonardi *et al.* (2015) have shown that transversal square bars can almost duplicate the smooth wall heat flux for pitch-to-height ratio $p/k \gtrsim 6$.

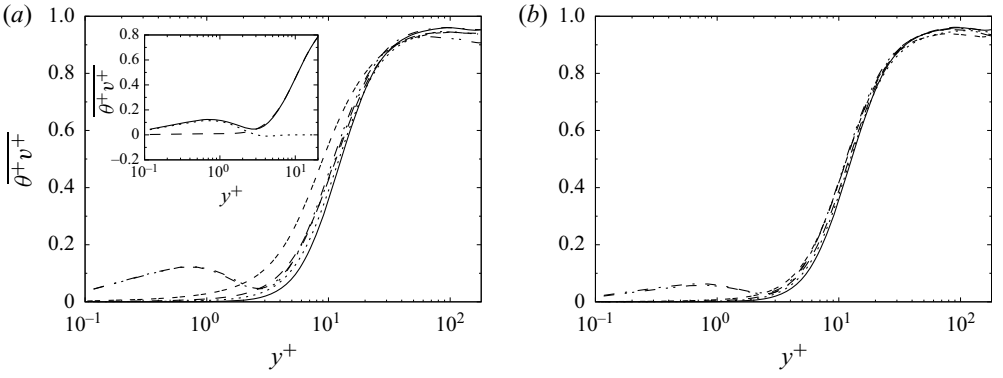

FIGURE 5. Convective heat flux $\overline{\theta^+ v^+}$ for SHS (*a*) and LIS (*b*): ——— smooth channel; ····· longitudinal ridges, $p/k = 2$; – – – – longitudinal ridges, $p/k = 4$; – – – – longitudinal ridges, $p/k = 8$; —·— transversal bars, $p/k = 2$; —··— transversal bars, $p/k = 4$. The inset in (*a*) shows the decomposition in turbulent component $\overline{\theta' v'}$ (– – – –) and dispersive component θv_{disp} (·····) of the total heat flux (———) for SHS transversal bars with $p/k = 4$.

The main contribution to the *HTE* derives from the turbulent convection due to the wall-normal velocity fluctuations (ejections). For smaller p/k, the flow tends to skim over the roughness elements decreasing the probability of ejections, thus achieving about the same heat transfer of the reference smooth wall. This latter flow pattern is similar to the present cases with LIS and SHS. The flat interface damps the wall-normal fluctuations from the substrate reducing the contribution of the turbulent heat convection despite the large pitch-to-height ratios (favourable for heat transfer enhancement).

Even though the heat flux is marginally reduced, the (normalized) heat flux to drag ratio, q/τ, improves compared to the smooth wall reference, figure 6. For a smooth wall, $q/\tau = 1$ owing to the Reynolds analogy (i.e. $St/(C_f/2) = 1$, Reynolds 1961; Kestin & Richardson 1963). We note that in practice different parameters may be used to measure the heat transfer efficiency depending on the particular application. Webb (1981) reviews some guidelines and examples to define performance evaluation criteria. In the present case, q/τ (or, equivalently, $St/(C_f/2)$) is the most suited parameter to compare against the smooth wall and study the Reynolds analogy over SHS and LIS. For LIS and SHS with longitudinal bars, q/τ is larger than one, meaning that these surfaces transfer heat more efficiently per unit drag. For transversal bars, q/τ is lower than one, which makes these surfaces similar to drag-increasing rough surfaces, for which also $q/\tau < 1$ (for instance, transversal square bars and rods considered in Leonardi *et al.* (2015)). However, the efficiency remains quite large ($q/\tau > 0.9$) compared to the values achieved by rough walls for the same pitch-to-height ratio. This is due to the damping of wall-normal fluctuations caused by the interface, which decreases the momentum transfer inside the substrate limiting the amount of drag increase (Arenas *et al.* 2019). Although this also reduces the enhanced turbulent thermal mixing, it appears that the effect is more prominent on the momentum balance rather than on the heat transfer.

The texture orientation seems to be the dominant parameter for the heat transfer efficiency. Using (3.3) and (3.15), it is possible to express the heat transfer efficiency as a function of the slip lengths:

$$\frac{q}{\tau} = \frac{1 + HTE}{1 - DR} = \frac{b^{+0} + Re/Re_{\tau,0}}{b_\theta^{+0} Pr + Re/Re_{\tau,0}} + f\left(\tilde{g}, \tilde{g}_\theta\right). \tag{3.18}$$

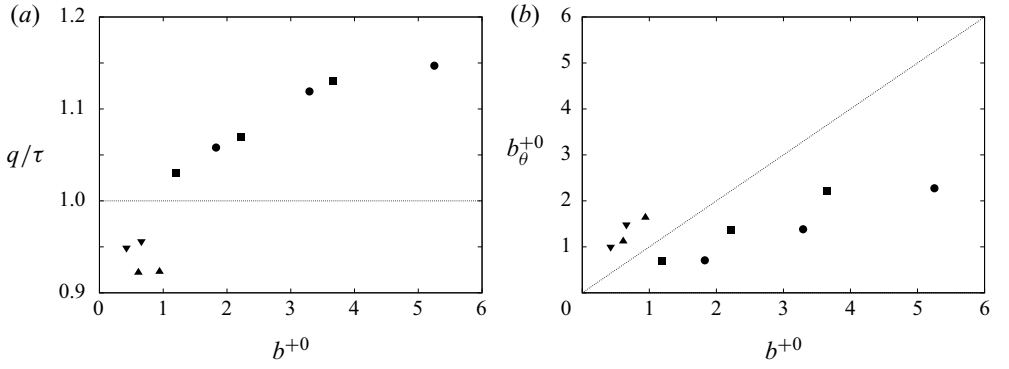

FIGURE 6. Heat transfer to drag ratio as a function of the streamwise slip length b^+ (a), and comparison between streamwise and thermal slip lengths (b). Longitudinal bars, $m = 0.01$ ● and $m = 0.4$ ■; transversal bars, $m = 0.01$ ▲ and $m = 0.4$ ▼.

In (3.18), f accounts for the contribution of turbulence and secondary motion to (3.3) and (3.15), that is the terms $\tilde{g}$ and $\tilde{g}_\theta$. In the case of $Pr = 1$ and neglecting $f(\tilde{g}, \widetilde{g_\theta})$, (3.18) indicates that the heat transfer efficiency is larger than unity if the streamwise slip length is larger than the thermal slip length, $b/b_\theta > 1$. Figure 6(b) compares the value of the slip lengths for the various cases and shows a good agreement with this criterion. Transversal textures, for which $q/\tau < 1$, are found above the main diagonal in the figure, thus $b < b_\theta$, while for longitudinal ridges, $b > b_\theta$ and $q/\tau > 1$. Results suggest the existence of a continuous transition from rough surfaces and transversal LIS/SHS ($q/\tau < 1$) to the smooth wall ($q/\tau = 1$), to longitudinal SHS/LIS ($q/\tau > 1$). This is corroborated by the recent study of Arenas *et al.* (2019), which establishes a common framework for LIS/SHS smooth and rough walls by identifying a unique scaling for the surface drag reduction or increase.

4. Effect of the interface dynamics

The case of a flat interface between the two fluids is an ideal scenario, which can only be asymptotically approximated with a very high surface tension between the fluids. In reality, the interface deforms causing non-zero wall-normal velocity fluctuations at the crest plane, which are critical for the momentum and thermal transport (Orlandi *et al.* 2003; Orlandi & Leonardi 2004). A set of DNS has been performed for $We^+ = 10^{-3}$ (approximately) using the level-set method to track the deformation of the interface and couple it to the momentum equations, as described in § 2. Table 2 reports the details on the interface deformation (and surface performance). The maximum mean deflection of the interface is computed from the level-set function as

$$\Delta_{max} = -\max_{x,z}[\langle \Phi \rangle (x, y_w, z)], \tag{4.1}$$

and maximum root-mean-square fluctuation as

$$\Delta_{rms} = \max_{x,z}\left[\sqrt{\langle \phi'\phi' \rangle (x, y_w, z)}\right]. \tag{4.2}$$

Here, Φ is the signed distance function from the interface, ϕ' is its fluctuation with respect to the phase average (denoted by the angle brackets, $\phi' = \Phi - \langle \Phi \rangle$); y_w indicates

Texture	m	p/k	Re_τ	We^+	Δ_{max}/k	Δ_{rms}/k	DR (%)	HTE (%)	q/τ	b^+	b_θ^+
Longitudinal	0.01	2	179.3	1.02×10^{-3}	−0.089	0.152	+0.9	+5.9	1.07	1.60	0.87
Longitudinal	0.01	4	174.6	0.99×10^{-3}	−0.129	0.183	+6.0	+5.0	1.12	2.65	1.53
Longitudinal	0.4	2	172.8	0.98×10^{-3}	−0.040	0.043	+8.0	−3.4	1.05	1.19	0.80
Longitudinal	0.4	4	169.0	0.96×10^{-3}	−0.094	0.088	+11.9	−4.7	1.08	1.98	1.43
Transversal	0.01	2	184.7	1.05×10^{-3}	−0.025	0.027	−5.1	0.0	0.95	0.37	0.70
Transversal	0.01	4	190.8	1.08×10^{-3}	−0.060	0.140	−12.2	+7.5	0.96	0.55	1.04
Transversal	0.4	2	185.4	1.05×10^{-3}	−0.024	0.017	−5.9	+2.9	0.97	0.28	0.72
Transversal	0.4	4	182.2	1.03×10^{-3}	−0.031	0.049	−2.3	−2.8	0.95	0.48	1.05

TABLE 2. Summary of surface performances for $We^+ = \mu_2 u_\tau/\sigma \simeq 10^{-3}$; Δ_{max} and Δ_{rms} are, respectively, the maximum mean and root-mean-square deflection of the interface, computed from the level-set function as $\Delta_{max} = -\max_{x,z}[\langle\Phi\rangle(x, y_w, z)]$, and $\Delta_{rms} = \max_{x,z}[\sqrt{\langle\phi'\phi'\rangle(x, y_w, z)}]$. A negative value of Δ_{max} indicates a downward displacement of the interface (towards the bottom of the cavity).

the crest plane. Therefore, $\Phi(x, y_w, z)$ quantifies the deflection of the interface from its initial position (flat interface at $y = y_w$). According to the definition of Φ, a positive value ($\Phi(x, y_w, z) > 0$) indicates that the interface is displaced downward (hence, the minus sign in (4.1) for a more intuitive definition of the sign of the displacement). As expected, the mean deformation and its fluctuation increase with p/k. This is consistent with the recent analysis of García Cartagena *et al.* (2019). They have shown that, for a substrate made of randomly disposed pinnacles, the mean interface displacement scales roughly linearly with the distance among the points where the interface is pinned (this would be equivalent to the cavity width for a texture of regularly placed bars as considered herein). In the present cases, the maximum displacement is ∼1 wall unit for cavity widths $p^+ \approx 18$–36, which is in close agreement with the magnitude reported by García Cartagena *et al.* (2019) for the same Reynolds and Weber numbers ($\Delta_{max}^+ \approx 1.5$ for widths of about 40 wall units).

Figure 7 shows the DR as a function of the streamwise slip length (defined as in (3.1)). Results for $We^+ = 10^{-3}$ are represented as empty symbols connected to the corresponding flat interface case to show the effect of the transition to a finite value of surface tension.

The effect on DR is quite different depending on the viscosity ratio. For SHS longitudinal bars, there is a considerable decline in the amount of DR. For the shortest pitch ($p/k = 2$), the surface generates essentially the same drag of the smooth wall, while for $p/k = 4$, more than half of DR amount is lost. Instead, LIS bars are not strongly affected by the change in the surface tension and maintain approximately the same amount of DR as in the ideal case. The interface of LIS is more robust to the overlying coherent structures and pressure fluctuations than SHS. Figure 8 shows the mean velocity profile for super-hydrophobic and liquid-infused longitudinal bars with $p/k = 4$ in the cases $We = 0$ and $We^+ = 10^{-3}$. Even in the case of $We = 0$, the velocity profiles for LIS and SHS in the cavity are qualitatively different. In these cases the flow in the cavity is mostly driven by the shear of the main fluid, and the velocity profiles show characteristics of shear-driven flows (other textures may result in a pressure-driven flow). Consistently, the velocity profile for LIS can be approximated with a linear velocity profile typical of a laminar Couette flow. For SHS, the motion in the cavity is mostly shear-driven as well, but in this case the profile assumes the shape of a turbulent Couette flow. Since the secondary fluid for SHS is less viscous, the cavity Reynolds number is larger than in the case of LIS. For the texture in

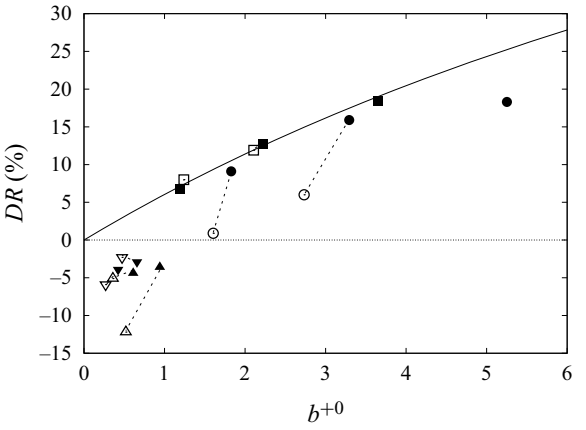

FIGURE 7. Drag reduction as a function of the slip length in 'nominal' wall units: longitudinal bars, $m = 0.01$ ● and $m = 0.4$ ■; transversal bars, $m = 0.01$ ▲ and $m = 0.4$ ▼. Solid symbols, $We = 0$; empty symbols, $We^+ = 10^{-3}$. Solid line, (3.3).

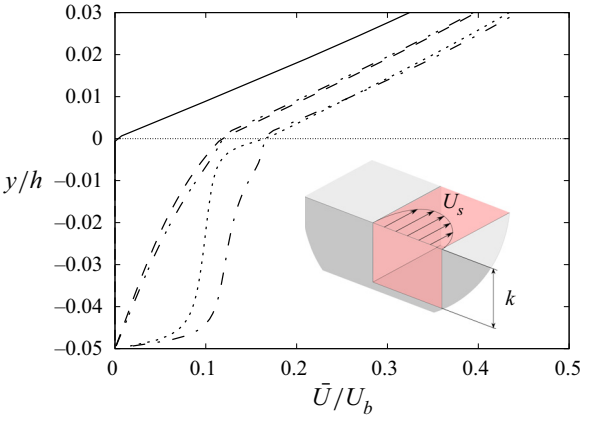

FIGURE 8. Mean velocity $\bar{U}$ profile near the interface ($y/h = 0$) for longitudinal ridges with $p/k = 4$. Super-hydrophobic surfaces ($m = 0.01$): ····· $We = 0$; —·— $We^+ = 10^{-3}$. Liquid-infused surfaces ($m = 0.4$): - - - - $We = 0$; —··— $We^+ = 10^{-3}$. Smooth channel case: ———.

the figure ($m = 0.01$, $p/k = 4$, $We = 0$), the Reynolds number for the flow in the cavity is

$$Re_{cav} = \frac{\rho \bar{U}_s k}{4\mu_1} \approx 600. \tag{4.3}$$

Here, the Reynolds number is defined as normally done for Couette flows with $k/2$ and half the velocity difference $\bar{U}_s/2$ (see the inset in figure 8 for the definitions). The value is larger than the transitional Reynolds number for which turbulence can be sustained in a Couette flow ($Re_{trans} = 360$; see e.g. Lundbladh & Johansson 1991; Tillmark & Alfredsson 1992; Komminaho, Lundbladh & Johansson 1996). Figure 9 shows second-order turbulence

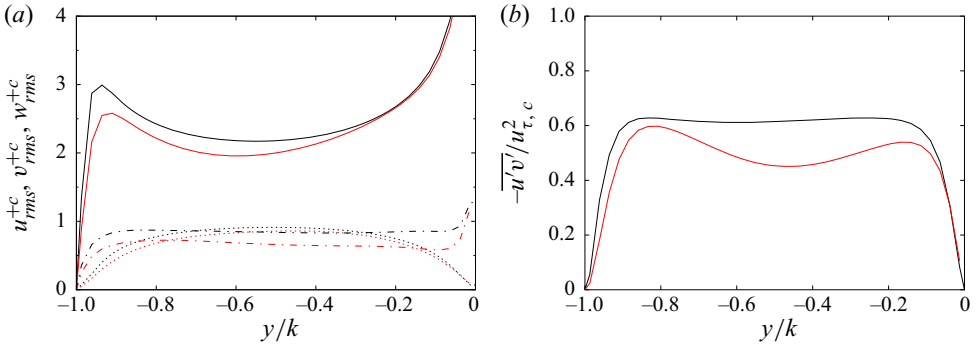

FIGURE 9. Turbulence statistics in the cavity for SHS longitudinal bars with $p/k = 4$ (black lines) and $p/k = 2$ (red lines). (*a*) Root-mean-square velocity fluctuations: ——— $u^{+c}_{rms} = \overline{u'u'}^{1/2}/u_{\tau,c}$; ····· $v^{+c}_{rms} = \overline{v'v'}^{1/2}/u_{\tau,c}$; —·— $w^{+c}_{rms} = \overline{w'w'}^{1/2}/u_{\tau,c}$. (*b*) Reynolds shear stress $-\overline{u'v'}$.

statistics in the cavity. Results are devoid of the dispersive component and normalized with a cavity friction velocity:

$$u_{\tau,c} = \sqrt{\frac{\tau_c}{\rho}} = \sqrt{\frac{1}{\rho}\mu_1 \left.\frac{\mathrm{d}\bar{U}}{\mathrm{d}y}\right|_{y=-k}}. \tag{4.4}$$

The side walls are not included in the definition of $u_{\tau,c}$, because, as suggested by studies in duct flows (Gavrilakis 1992; Vinuesa *et al.* 2014; Pirozzoli *et al.* 2018; Orlandi & Pirozzoli 2020*a*,*b*), the 'local' friction (as opposed to the total friction) is the appropriate scaling for one-point turbulence statistics (we remind the reader that this is related to the analysis of the cavity and the definition of $u_{\tau,c}$ only; the friction on all walls is considered in the overall u_τ for the surface used in the preceding and following sections). The velocity fluctuations are consistent with the typical behaviour of Couette flow turbulence in the lower half of the cavity ($y/k < -0.5$). Approaching the crest plane ($y/k = 0$), the streamwise and spanwise components do not vanish, as it would occur for a physical wall, owing to the variations of the velocity at the interface and the overlying flow turbulence. Instead, the wall-normal component tends to zero as expected, because $V(y/k = 0) \equiv 0$ at the interface for $We = 0$. The Reynolds shear stress $\overline{u'v'}$ (figure 9*b*) shows the constant trend in the middle of the cavity typical of the turbulent Couette flow. The value in wall units is not closer to unity probably because of the presence of the side walls (which accounts for part of the friction). The results for the smaller cavity ($p/k = 2$) are also consistent with Couette flow turbulence. In this case the cavity Reynolds number is about the same as the transitional value ($Re_{cav} \approx 360$), and low-Reynolds effects are visible, for example, in the Reynolds shear stress distribution. At any rate, the intensity of this turbulent motion inside the cavity is low compared to the turbulence intensity in the main stream. The frictional Reynolds number $Re_{\tau,c} = \rho u_{\tau,c}(k/2)/\mu_1$ for the flow in the cavity is about 50 and 70 for $p/k = 2$ and $p/k = 4$, respectively. In the case of LIS the cavity Reynolds number $Re_{cav} = \rho \bar{U}_s k/4\mu_1 \approx 10$ is well below the transitional Reynolds number and the velocity in the cavity is closer to the laminar linear profile.

With the variation in surface tension, the velocity profile for LIS is largely unaltered apart from minor changes in the neighbourhood of the crest plane ($y/h = 0$). Conversely, in the case of super-hydrophobic surfaces, the velocity inside the cavity ($y/h < 0$)

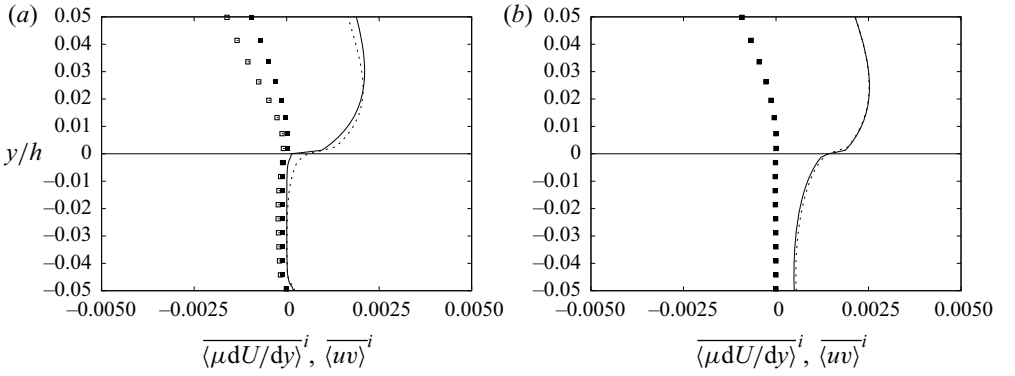

FIGURE 10. Shear stress balance for longitudinal bars, with $p/k = 4$ and $m = 0.01$ (*a*, SHS) and $m = 0.4$ (*b*, LIS). Lines are for the viscous shear stress, symbols (plotted every 4 points, for clarity) are for the Reynolds stress $\langle uv \rangle$. Solid lines and symbols (———, ■) denote $We = 0$ cases, dashed lines and empty symbols (– – – –, □) are for the $We^+ = 10^{-3}$ cases.

increases considerably for $We^+ = 10^{-3}$. When the interface deforms ($We^+ = 10^{-3}$), more momentum is transferred (and dissipated) inside the cavities by the Reynolds stress $\overline{uv}$ at the interface, which decreases the amount of *DR* (Arenas *et al.* 2019). The momentum balance in the cavity for super-hydrophobic and liquid-infused surfaces has been analysed in detail by Arenas *et al.* (2019). The conditions at the interface determine the drag in the cavity, as they have shown integrating the momentum (2.2) over the volume of the cavity:

$$\int_{S_{int}} \left[\frac{1}{Re} \frac{\mathrm{d}\langle U \rangle}{\mathrm{d}y} - \langle uv \rangle \right] \mathrm{d}S + \langle \Pi \rangle V_t = \int_{S_{cav}} \frac{m}{Re} \frac{\mathrm{d}\langle U \rangle}{\mathrm{d}n} \mathrm{d}S. \tag{4.5}$$

Here S_{int} is the surface of the interface between the two fluids, S_{cav} is the surface of the cavity and V_t is the volume of the cavity. The drag in the cavity, i.e. the right-hand side of the equation, has no form drag component for the case of longitudinal bars. Equation (4.5) is applicable also for $We \neq 0$ if the interface deformation is small, which is appropriate for the present textures (table 2). Figure 10 shows the viscous and Reynolds shear stresses for SHS and LIS longitudinal bars with $p/k = 4$. Following (4.5), the stresses are averaged over the interface (denoted with the overline and superscript i). For SHS, in the case of $We^+ = 10^{-3}$ both the viscous stress and the Reynolds stress increase compared to the flat interface case. This increases the shear-driven momentum in the cavity, and eventually the drag as quantified by (4.5). In the case of LIS the discrepancy between the $We^+ = 0$ and $We^+ = 10^{-3}$ cases is negligible and, consistently, the profiles in figure 8 essentially collapse onto each other.

For transversal bars, the finite surface tension slightly reduces the yet modest streamwise slip length. The drag is also marginally affected, except for the SHS case with the largest pitch-to-height ratio ($p/k = 4$), for which drag is increased. This case approaches to the rough wall scenario, where, for large p/k values, strong $\overline{uv}$ events contribute to intensify and maximize drag increase (Leonardi *et al.* 2003).

The effect on the heat transfer enhancement and thermal slip length is shown in figure 11(*a*). The thermal slip length tends to be smaller than one viscous unit ($b_\theta^{+0} \lesssim 1$, see also table 2) for transversal bars, while it does not significantly change for longitudinal bars. A general increase in the heat flux is observed. For SHS textures, particularly, this is

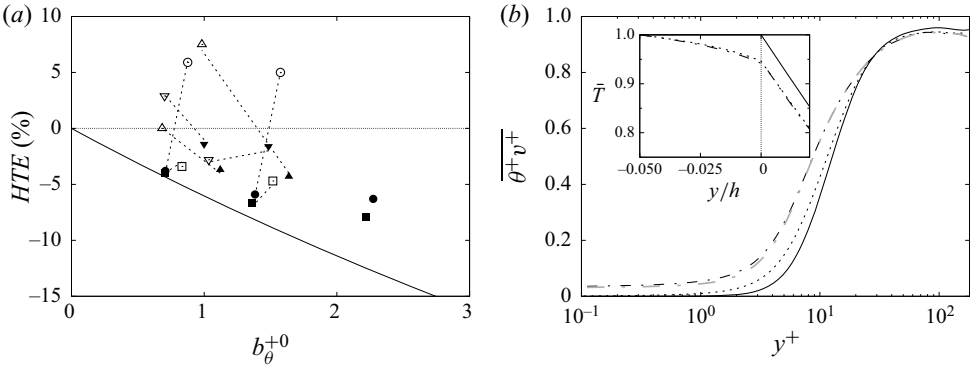

FIGURE 11. (*a*) Heat transfer enhancement as a function of b_θ^{+0}: longitudinal bars, $m = 0.01$ • and $m = 0.4$ ■; transversal bars, $m = 0.01$ ▲ and $m = 0.4$ ▼. Solid symbols, $We = 0$; empty symbols, $We^+ = 10^{-3}$. Solid line, (3.15). (*b*) Total convective heat flux $\overline{\theta^+v^+}$ for SHS longitudinal ridges with $p/k = 4$, $m = 0.01$: ····· $We = 0$; —·— $We^+ = 10^{-3}$; ——— smooth channel. The grey thick line (—·—, grey) shows the turbulent component $\overline{\theta'v'}$ for the $We^+ = 10^{-3}$ case. The inset shows the mean temperature profile $\bar{T}$ near the substrate.

sufficient to achieve a positive *HTE*, meaning that the surface sustains a larger heat flux than the smooth wall, whereas in the ideal flat interface scenario $HTE < 0$ for all surfaces. The main mechanism for the performance enhancement is the generation of $\overline{\theta v}$ flux at the interface. Figure 11(*b*) shows as an example the convective flux and the mean temperature profile (inset) for one case with $HTE > 0$. The mean profile $\bar{T}$ is not significantly changed following the variation in Weber number, particularly the gradient at the interface, which determines the molecular heat flux. However, for $We^+ \neq 0$, the total heat flux is the sum of the molecular heat flux and the convective contribution, which does not vanish as for the infinite surface tension case. This is evident from the $\overline{\theta v}$ profile. The enhancement in the convective flux is mainly due to the turbulent heat flux (shown with the grey thick line in figure 11*b*). The dynamics of the interface allows the generation of wall-normal fluctuations and turbulent transport at the crest plane, whereas this mechanism is damped when $We = 0$.

The turbulent heat flux $\langle\theta'v'\rangle$ is also visualized in figure 12 for longitudinal bars with $p/k = 4$. Super-imposed vorticity contours indicate the presence of counter-rotating vortex pairs. This flow pattern over longitudinal SHS/LIS has been documented by Arenas *et al.* (2019), which have compared it to the analogous flow structures observed at the tip of riblets. Longitudinal streamwise vortices, also generated over ribbed channels, are beneficial for heat transfer improvement (Hetsroni *et al.* 1999; Miyake *et al.* 2001; Leonardi *et al.* 2004). The intensity of the vortices is larger for SHS than LIS. In addition, the vortical motion in the cavities is stronger for SHS, which is a consequence of the local turbulent motion for this texture. With $We^+ = 10^{-3}$, the vortices intensify and the downwash in the middle of the cavity induces a mean downward displacement of the interface. This secondary motion affects the distribution of $\langle\theta'v'\rangle$, and results in a clear increase of the turbulent heat flux for $m = 0.01$. In fact, this texture has a $HTE > 0$. Transversal bars present a much weaker secondary motion and are not shown here.

As a result of the interface deformation and the increased fluxes at the crest plane, the correlation between *HTE* and b_θ is almost lost. This is the case also for drag reduction

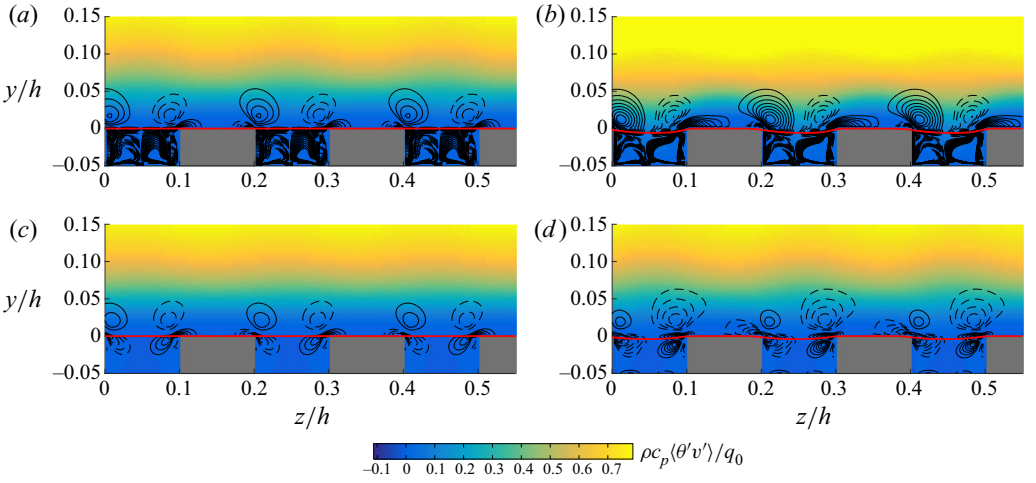

FIGURE 12. Turbulent heat flux $\langle\theta' v'\rangle$ with superimposed streamwise vorticity $\langle\Omega_x\rangle$ contours (———$\langle\Omega_x\rangle > 0$; - - - -$\langle\Omega_x\rangle < 0$) for longitudinal bars with $p/k = 4$. Top row (*a*,*b*): $m = 0.01$ (SHS); bottom row (*c*,*d*): $m = 0.4$ (LIS). Left (*a*,*c*), $We = 0$; right (*b*,*d*), $We^+ = 10^{-3}$. Contour lines every 0.025 for SHS, and every 0.015 for LIS. The thick red line denotes the mean interface position.

and streamwise slip length (figure 7). The common reason is that, in the presence of a deformable interface, the slip conditions at the interface are no longer the sole or dominant factor for either drag reduction or heat transfer enhancement. Wall-normal velocity fluctuations lead to the generation of Reynolds shear stresses $\overline{uv}$ and fluxes $\overline{\theta v}$. The terms $\tilde{g}$ and $\tilde{g}_\theta$ in (3.3) and (3.15) acquire increasing importance, which leads to the departure from the pure 'slip' behaviour.

The heat transfer efficiency q/τ and the slip length comparison for the $We^+ = 10^{-3}$ cases are shown in figure 13. For transversal bars, the ratio b/b_θ tends to the main diagonal, $b = b_\theta$. Consistently with (3.18), the heat transfer efficiency for these textures tends to the smooth wall value, $q/\tau = 1$. Analogously, q/τ is generally increased, and remains above 1, for the cases with longitudinal orientation, for which $b > b_\theta$. Thus, the results for the deformable interface case have a good agreement with (3.18), although this expression was derived neglecting turbulent and secondary motions in the channel. These motions become more important for finite surface tension (see, for example, the departure from the analytical trends in figures 2 and 3). However, since their effect is to increase (with respect to the $We = 0$ case) both q and τ (figures 7 and 11), their impact on the ratio q/τ approximately cancels out.

Compared to the ideal flat interface case, the efficiency is improved for essentially all the geometries. In particular, SHS longitudinal textures achieve $q/\tau > 1$ by simultaneously reducing drag and increasing the heat transfer rate. This leads to an apparent breakdown of the Reynolds analogy, understood in a broad sense as the inevitable correlation between heat transfer enhancement and drag increase. In reality, this is justified by the original lack of similarity between the thermal and momentum balance in the governing equations (2.2) and (2.3). With respect to the classical case (Teitel & Antonia 1993), the different properties of the two fluids and the presence of the interface between them are reflected in a different way in the balance equations. In addition, the textured two-fluid configuration of LIS and SHS involves additional sources of energy-momentum dissimilarity. The surface

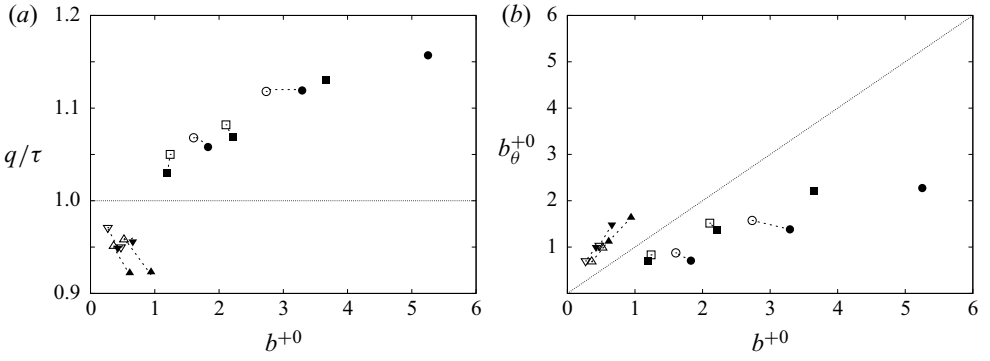

FIGURE 13. Heat transfer to drag ratio as a function of the streamwise slip length b^{+0} (*a*), and comparison between streamwise and thermal slip lengths (*b*). Longitudinal bars, $m = 0.01$ ● and $m = 0.4$ ■; transversal bars, $m = 0.01$ ▲ and $m = 0.4$ ▼. Solid symbols, $We = 0$; empty symbols, $We^+ = 10^{-3}$.

Texture	m	a	p/k	Re_τ	We^+	Pr	DR (%)	HTE (%)	$\frac{q}{q_0}\frac{\tau_0}{\tau}$	b^+	b_θ^+
Riblets	—	—	2	178.8	—	1	+0.7	−2.5	0.98	0.36	0.64
Longitudinal	1	1	2	177.0	0	1	+3.5	−3.8	1.00	0.76	0.69
Longitudinal	1	1	2	175.1	0.99×10^{-3}	1	+4.9	−4.4	1.01	0.82	0.91
Longitudinal	0.4	0.23	4	167.7	0	1	+13.0	−9.1	1.04	2.07	2.27
Longitudinal	0.01	0.04	4	164.2	0	1	+16.6	−11.6	1.06	3.02	2.82
Longitudinal	0.4	0.23	4	167.3	0	7	+13.7	−16.0	0.98	2.10	2.06
Longitudinal	0.01	0.04	4	163.7	0	7	+17.4	−14.8	1.03	3.00	1.91

TABLE 3. Parametric study on fluid properties: summary of surface performance. The 'riblets' case indicates longitudinal bars with $p/k = 2$ and one fluid only. The heat transfer statistics for $Pr = 7$ cases are computed with respect to a smooth channel with one fluid and $Pr = 7$.

tension force f_i in (2.2) has no counterpart in the energy equation. Likewise the pressure term, which may be significant in the substrate (Arenas *et al.* 2019), affects only the momentum equation. In summary, the physical mechanisms involved in non-canonical wall-bounded flows such as LIS and SHS provide novel potential for so-called 'dissimilar control' (Hasegawa & Kasagi 2011; Kasagi *et al.* 2012), i.e. the simultaneous drag reduction and heat transfer increase.

5. Effect of fluid properties

Different viscosity and/or diffusivity ratios a and m will affect the transport mechanisms over the surface, changing the thermal and momentum balance. In this section we analyse the sensitivity to the fluid properties of the surface performance. Table 3 summarizes the cases considered for this parametric study.

In terms of drag reduction, Fu *et al.* (2017) have analysed to a great extent its dependence upon the viscosity ratio m in the case of $We = 0$, noting that $DR > 0$ even for $m \approx O(1)$.

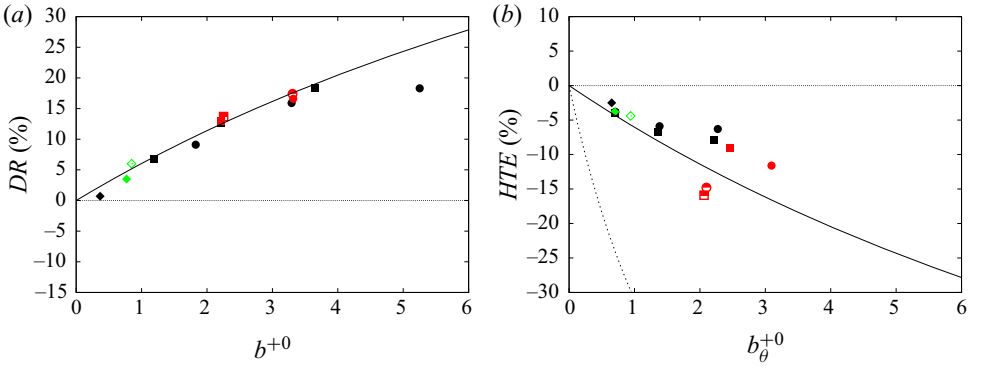

FIGURE 14. Drag reduction (a) and heat transfer enhancement (b) as a function of the slip lengths (b and b_θ, respectively) in 'nominal' wall units for longitudinal bars. Symbols (as in figure 2): $m = 0.01$ • and $m = 0.4$ ■. Additional cases in table 3: $m = 1$ ♦ (green) (solid, $We = 0$; empty, $We^+ = 10^{-3}$); 'riblets' ♦ (black). Red symbols (■, •) denote the change in diffusivity ratio a: solid symbols, $Pr = 1$; half-solid, $Pr = 7$. Lines: (a) (3.3) with $\tilde{g} \equiv 0$; (b) ——— equation (3.15) with $\tilde{g}_\theta \equiv 0$ and $Pr = 1$; ····· (3.15) with $\tilde{g}_\theta \equiv 0$ and $Pr = 7$.

As recently clarified by Arenas *et al.* (2019), the interface enables *DR* even when the infused liquid has a viscosity of the same order of the primary fluid, by suppressing wall-normal velocity fluctuations. Present results for $m = 1$ and $We = 0$ are consistent with these previous studies (figure 14). In addition, the *DR* is larger than what is obtained when the same texture (longitudinal bars with $p/k = 2$) is wet by the primary fluid only. As explained by Arenas *et al.* (2019), this is due to the interface, which avoids the typical failure mechanism of riblets with the secondary streamwise vortices (such as those in figure 12) penetrating inside the cavities. The deformation of the interface ($We^+ = 10^{-3}$ case) does not change much the drag reduction performance. As explained above comparing LIS ($m = 0.4$) and SHS ($m = 0.01$), a large viscosity of the fluid in the cavity damps the momentum transfer from the primary fluid and avoids the generation of strong wall-normal velocity fluctuations, which would reduce the amount of *DR*. The thermal performance is also very similar among these textures and scales well with the thermal slip length (figure 14*b*). The observed reduction in heat flux for 'riblets' corroborates findings from previous studies (Stalio & Nobile 2003; Orlandi *et al.* 2016).

As it could be expected, the *HTE* is more sensitive to the variation in the thermal diffusivity ratio $a = \alpha_1/\alpha_2$, rather than the diffusivity ratio. Two values of a have been considered, $a = 0.04$ and $a = 0.23$, to mimic the conductivity ratio of water over air and water over heptane, respectively. With the reduction in the thermal diffusivity of the secondary fluid, compared to reference case $a = 1$, the heat flux carried in the cavity decreases. This results in larger thermal slip length b_θ and lower slip temperature $\bar{T}_s$. The total heat transfer rate decreases by about 10 %, especially for SHS ($m = 0.01$) because of the low thermal conductivity. The decrease in *HTE* is consistent with (3.15), although the contribution of turbulence and secondary motion in the overlying channel is larger than for the same geometry ($p/k = 4$) and $a = 1$. This can be expected since the larger heterogeneity at crest plane (i.e. larger $T_w - \bar{T}_s$) leads to a larger dispersive flux partly compensating for the reduction in molecular heat flux in the cavity.

According to (3.15), an increase in the Prandtl number of the primary fluid ($Pr = \nu_2/\alpha_2$) leads to a comparatively larger downgrade in *HTE* compared to the unitary Prandtl number

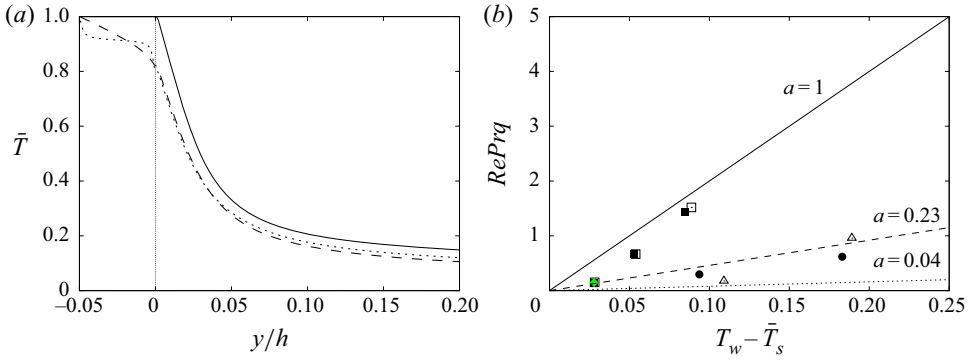

FIGURE 15. (*a*) Temperature profile for the $Pr = 7$ cases near the crest plane ($y/h = 0$): ——— smooth wall; – – – – $m = 0.4$ and $a = 0.23$ (LIS); ····· $m = 0.01$ and $a = 0.04$ (SHS). (*b*) Non-dimensional heat flux as a function of $T_w - \bar{T}_s$ for all the $We = 0$ cases with longitudinal bars. Solid symbols denote LIS textures ($m = 0.4$), empty symbols are for SHS ($m = 0.01$). Diffusivity ratios: $a = 1$ ■; $a = 0.23$ ●; $a = 0.04$ ▲. The case $m = 1$ and $a = 1$ is denoted with ♦ (green). Lines: (5.1) with $a = 1$ (———); $a = 0.23$ (– – – –); $a = 0.04$ (·····).

case for a given thermal slip length. Two simulations have been performed for $Pr = 7$, which is approximately the value for water as a working fluid. The value of *HTE* is effectively reduced for both LIS and SHS. However, the reduction compared to the smooth wall is significantly less than what would be predicted by the slip contribution only. The thickness of the thermal boundary layer reduces for high-Pr fluids, and near-wall turbulent coherent structures can mix fluid in a layer with low thermal resistance. Therefore, the importance of turbulent convection increases, which explains the larger discrepancy from the slip trend of (3.15).

In addition, the SHS texture ($m = 0.01$, $Pr = 7$) yields a larger heat flux than the LIS case, despite the fluid in the cavity having a much lower diffusivity. Turbulent heat transport ($\overline{\theta v}$) also occurs in the cavity for this texture. Figure 15(*a*) shows the mean temperature profile for the $Pr = 7$ simulations, which present a similar trend to the velocity profiles in figure 8. Because of the larger Prandtl number of the fluid in the cavity ($Pr_1 = \nu_1/\alpha_1 = Pr\,m/a$), the temperature profile also assumes a characteristic turbulent shape (as opposed to the inset in figure 11*b*). Owing to the additional turbulent contribution, the fluid in the cavity is able to carry a larger heat flux than with conduction only. In that case, the heat flux in non-dimensional form could be expressed as

$$q = \frac{a}{RePr}\frac{T_w - \bar{T}_s}{k}, \tag{5.1}$$

with k being the cavity height. Figure 15(*b*) shows that all textures follow with a close approximation (5.1). The data points lie below the curve because (5.1) does not account for the lateral walls in the cavity, but is just based on one-dimensional conduction. The only exceptions to this trend are represented by the SHS textures with $a = 0.04$, and notably for the $Pr = 7$ case (the $Pr = 1$ case also presents a moderate turbulent 'S'-profile).

Figure 16 shows the heat transfer efficiency. The results are presented as $(q/q_0) \cdot (\tau_0/\tau)$ because for $Pr = 7$ the non-dimensional heat flux to drag ratio is $q/\tau \approx 0.3$, in fairly good agreement with the Colburn analogy factor ($q/\tau = 2St/C_f = Pr^{-2/3}$; Colburn 1964). The case $m = 1$ is close to the LIS texture with the same geometry (p/k) both for $We = 0$ and

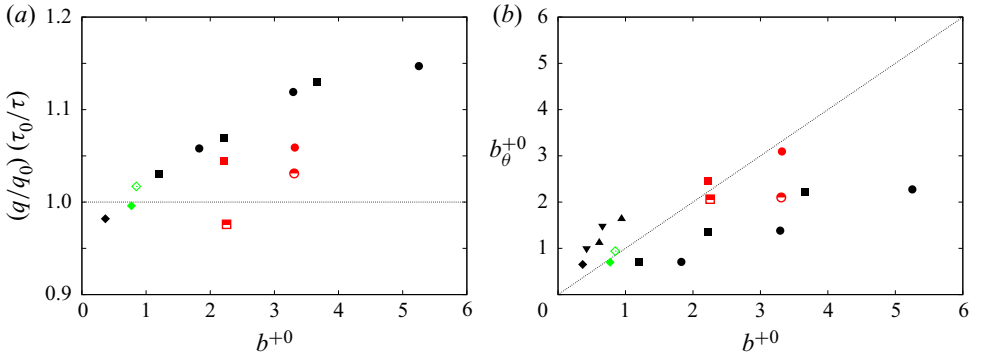

FIGURE 16. Heat transfer to drag ratio as a function of the streamwise slip length b^{+0} (*a*), and comparison between streamwise and thermal slip lengths (*b*). Symbols as in figure 14.

$We = 10^{-3}$, which is consistent with the general trends discussed in §§ 3 and 4, for textures with high-viscosity secondary fluid. For the values considered in this study, the variation in the diffusivity ratio a tends to reduce the heat flux to drag ratio. This is because the drag is not affected by the value of a, since the temperature is treated as a passive scalar (in fact, the textures have, approximately, the same drag and slip length for different values of a). On the other hand, the heat transfer rate is reduced because of the reduced thermal capacity in the cavities. Figure 16(*b*) supports to a good approximation the correlation derived in (3.18) between $b/b_\theta > 1$ and $q/\tau > 1$.

6. Conclusion

Direct numerical simulations of a turbulent channel flow with two superposed fluids have been performed. The second fluid fills cavities in the lower wall made of either longitudinal or transversal bars with different pitch-to-height ratio (p/k). Two viscosity ratios between the two fluids are used to mimic idealised super-hydrophobic and liquid-infused surfaces. Two cases have been considered for the interface between the two fluids: (i) the ideal scenario of infinite surface tension, in which the interface remains flat and slippery in the wall-parallel directions; and (ii) a finite value of surface tension ($We^+ = 10^{-3}$), for which the interface can dynamically deform depending on the fluids motion. The two walls (textured lower wall and smooth upper wall) are kept at two different temperatures to study the heat transfer characteristics.

The present simulations confirm the observed trends in the literature regarding the drag-reducing capabilities of LIS and SHS. Compared to the equivalent channel with both smooth walls, drag reductions up to about 20 % are obtained using longitudinal ridges if the interface remains flat. The drag reduction increases with increasing pitch between the textures and is larger for SHS than LIS. However, for a finite value of the surface tension, the amount of *DR* significantly drops for SHS. In fact, more momentum is transferred in the cavity in the SHS case, which leads to larger drag of the fluid in texture and less *DR*. The flow in the cavity for SHS has the characteristics of a turbulent Couette flow, rather than a laminar shear-driven flow, due to the larger cavity Reynolds number. Because of the larger viscosity of the fluid in the cavity, LIS are more robust to the dynamics of the interface and are able to maintain about the same level of the drag reduction as in the ideal $We = 0$ case.

In presence of a flat interface, the heat transfer is generally reduced by 5–10 % compared to the smooth wall case for the considered geometries. A model has been analytically derived from the energy equation, which correlates the heat transfer enhancement (*HTE*) with the thermal slip length, in analogy with the scaling between streamwise slip length and drag reduction. From simulation results, a good correlation is observed as long as the thermal slip length, scaled in wall units, is small ($b_\theta^+ \lesssim 1$), corresponding to low-to-moderate p/k values. For larger p/k, the secondary motion induced by the texture increases in intensity, and the thermal slip length is no longer the dominant parameter for the heat transfer performance. In the case of a deformable interface, non-vanishing turbulent fluxes at the interface further reduce the correlation between *HTE* and b_θ. These fluxes increase the heat transfer rate, which for super-hydrophobic textures is larger than the smooth wall baseline.

A parametric study on the effect of the fluid properties has been performed. The amount of *HTE* tends to decrease with the reduction of the diffusivity of the fluid in the cavity. Super-hydrophobic surfaces are in principle more penalized than LIS, because of the low conductivity of air. However, depending on the flow conditions, the turbulent motion in the cavity of SHS leads to an enhanced convective flux which compensates and may overcome the loss in conductive heat transfer.

The relative magnitude of the streamwise and thermal slip lengths (b/b_θ) is found to be a good parameter to scale the (non-dimensional) heat transfer efficiency (q/τ), in accordance with the analytical model proposed here for heat transfer and the model of Rastegari & Akhavan (2015) for drag reduction. Longitudinal textures present a value of q/τ larger than unity (which is the smooth wall value owing to the Reynolds analogy). Correspondingly, for these textures, the streamwise slip length is larger than the thermal slip length. Transversal bars have q/τ slightly lower than one and the thermal slip length is larger than the streamwise slip length. The scaling of q/τ with b/b_θ holds for both transversal and longitudinal textures also in the case of a finite surface tension and deformable interface. Results suggest the existence of a continuous trend from either rough surfaces or transversal SHS/LIS ($q/\tau < 1$) to the smooth wall ($q/\tau = 1$) and to streamwise LIS/SHS ($q/\tau > 1$) also for heat transfer, in analogy with the unique scaling for drag recently found by Arenas *et al.* (2019). In addition, in the case of finite surface tension, longitudinal SHS textures show simultaneous drag reduction and heat transfer enhancement. This apparent breakdown in the Reynolds analogy is caused by the 'controlled' fluctuations of the interface, which damps without completely suppressing wall-normal velocity fluctuations responsible for the Reynolds stresses and turbulent convective fluxes. The breakdown of the analogy is justified by the original lack of similarity in the momentum and thermal balance. The presence of the texture, the interface and the secondary fluid in LIS/SHS involves additional terms in the momentum equations, which have no symmetric counterpart in the energy equation.

Although this is still a fundamental study, the results are promising for practical applications. The use of LIS and SHS expands the control space for engineers. Instead of compromise solutions with *HTE* and proportional drag increase, with these surfaces it seems possible to tune *HTE* and *DR*. For instance, transversal bars increase the drag significantly when in a rough configuration (i.e. one fluid only and no interface). With an interface, in a LIS/SHS configuration, they still provide $HTE > 0$, but with a marginally larger drag than that over a smooth wall. Depending on the application, one can reach an optimal combination of heat transfer and drag by tuning the shape of the substrate and the viscosity and diffusivity ratios.

Texture	m	p/k	Re_τ	N_x	N_y	N_z	Δx^+	Δy^+_{min}	Δy^+_{max}	Δz^+	Id	$\frac{(\tau_1-\tau_i)}{\tau_1}$	$\frac{(q_1-q_i)}{q_1}$
L.B.	0.01	4	174.6	512	384	640	2.18	0.22	1.86	0.87	1	—	—
L.B.	0.01	4	173.3	1280	384	640	0.87	0.22	1.85	0.87	2	+1.47 %	+0.88 %
T.B.	0.01	4	190.8	1280	384	640	0.95	0.24	2.03	0.95	1	—	—
T.B.	0.01	4	189.9	2560	384	640	0.47	0.24	2.02	0.95	2	+0.92 %	+0.86 %

TABLE 4. Grid resolution for longitudinal bars (L.B.) and transversal bars (T.B.) with $We^+ = 10^{-3}$. A grid sensitivity analysis is shown for the drag and the heat flux at the textured wall.

Acknowledgements

This research was partially supported by ONR MURI grants N00014-12-01-0875 and N00014-12-01-0962, program manager Dr K.-H. Kim. Numerical simulations were performed on TACC systems.

Declaration of interests

The authors report no conflict of interest.

Appendix

For the cases with infinite surface tension ($We = 0$), the grid consists of $N_x \times N_y \times N_z = 512 \times 384 \times 640$ points in the streamwise, wall-normal and spanwise directions, respectively. The grid is uniform in the x–z plane and is stretched in the wall-normal direction, with 40 points clustered within the textures. Arenas *et al.* (2019) carried out a detailed grid sensitivity study with the present numerical method for various textures, including longitudinal and transversal bars. Compared to finest resolution tested in the appendix therein, the relative error for the present grid resolution in the prediction of the drag is less than 1 % for both viscosity ratios and both texture orientations. In addition, comparing results relative to different grids, only minor discrepancies are observed in the profiles of first- and second-order velocity statistics.

For the cases with finite surface tension ($We = 10^{-3}$), the same grid as the flat interface cases ($512 \times 384 \times 640$) is used for longitudinal bars. For transversal bars, 1280 grid points have been used in the streamwise direction to properly resolve the deformation of the interface on the windward side of the transversal bar. To assess the dependence of the results on grid resolution, two additional simulations have been performed for transversal and longitudinal bars with $m = 0.01$ and $p/k = 4$. For these cases, the resolution in the streamwise direction has been increased using 1280 and 2560 grid points for longitudinal and transversal bars, respectively. Table 4 reports the details of this grid sensitivity analysis. The discrepancy in the prediction of drag and heat flux is around 1–1.5 %. These values are lower than typical differences observed with respect to the smooth wall.

Mean velocity, temperature and turbulence intensity profiles are shown in figure 17. Results for the first-order statistics (mean velocity and temperature) depend weakly on the grid. The velocity fluctuations show an increased sensitivity, especially within the textures. Overall the agreement is acceptable, and the grid resolutions employed appear sufficient to support the main conclusions of the paper.

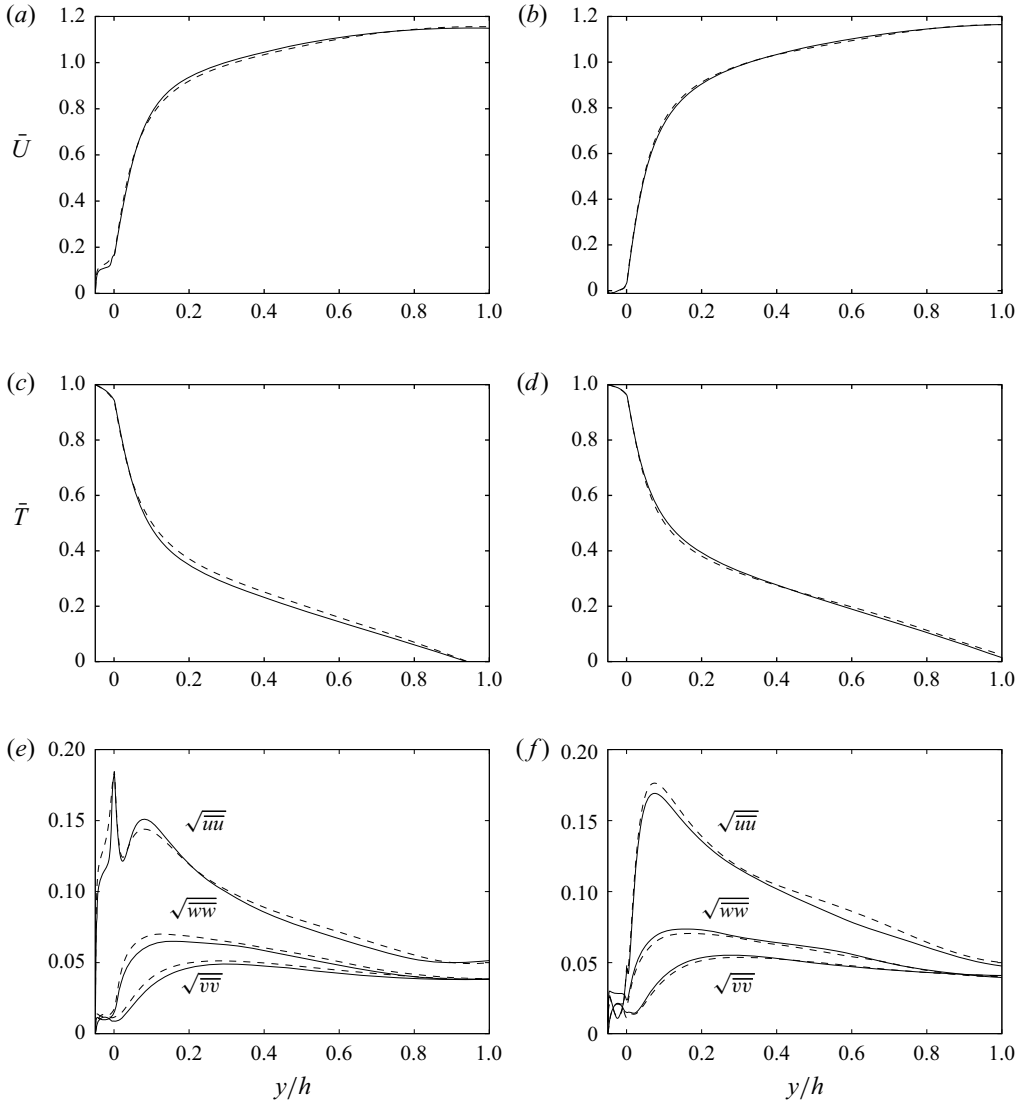

FIGURE 17. Streamwise velocity profile (*a*,*b*), temperature profile (*c*,*d*) and r.m.s. velocity fluctuations (*e*,*f*) for longitudinal bars (left, *a*,*c*,*e*) and transversal bars (right, *b*,*d*,*f*). Longitudinal bars: —— $1280 \times 384 \times 640$; - - - - $512 \times 384 \times 640$. Transversal bars: —— $2560 \times 384 \times 640$; - - - - $1280 \times 384 \times 640$. Velocities are normalized with the bulk velocity, temperature with the reference temperature (§ 2).

REFERENCES

ARENAS, I., GARCÍA, E., ORLANDI, P., FU, M. K., HULTMARK, M. & LEONARDI, S. 2019 Comparison between super-hydrophobic, liquid infused and rough surfaces: a direct numerical simulation study. *J. Fluid Mech.* **869**, 500–525.

BECHERT, D. W., HOPPE, G. & REIF, W.-E. 1985 On the drag reduction of the shark skin. *AIAA Paper* 85-0546.

BRACKBILL, J. U., KOTHE, D. B. & ZEMACH, C. 1992 A continuum method for modeling surface tension. *J. Comput. Phys.* **100**, 335–354.

CHANG, J., JUNG, T., CHOI, H. & KIM, J. 2019 Predictions of the effective slip length and drag reduction with a lubricated micro-groove surface in a turbulent channel flow. *J. Fluid Mech.* **874**, 797–820.

CHANG, Y. C., HOU, T. Y., MERRIMAN, B. & OSHER, S. 1996 A level set formulation of Eulerian interface capturing methods for incompressible fluid flows. *J. Comput. Phys.* **124**, 449–464.

CHENG, Y., XU, J. & SUI, Y. 2015 Numerical study on drag reduction and heat transfer enhancement in microchannels with superhydrophobic surfaces for electronic cooling. *Appl. Therm. Engng* **88**, 71–81.

CHOI, H., MOIN, P. & KIM, J. 1993 Direct numerical simulation of turbulent flow over riblets. *J. Fluid Mech.* **255**, 503–539.

CHOI, K.-C. & ORCHARD, D. M. 1997 Turbulence management using riblets for heat and momentum transfer. *Exp. Therm. Fluid Sci.* **15**, 109–124.

COLBURN, A. P. 1964 A method of correlating forced convection heat-transfer data and a comparison with fluid friction. *Intl J. Heat Mass Transfer* **7**, 1359–1384 (reprinted from *Trans. Amer. Inst. Chem. Engrs.*, 29, pp. 174–209, 1933).

DANIELLO, R. J., WATERHOUSE, N. E. & ROTHSTEIN, J. P. 2009 Drag reduction in turbulent flows over superhydrophobic surfaces. *Phys. Fluids* **21** (8), 085103.

ENRIGHT, R., HODES, M., SALAMON, T. & MUZYCHKA, Y. 2014 Isoflux Nusselt number and slip length formulae for superhydrophobic microchannels. *Trans. ASME: J. Heat Transfer* **136**, 012402.

EKKAD, S. V. & HAN, J. C. 1997 Detailed heat transfer distributions in two-pass square channels with rib turbulators. *Intl J. Heat Mass Transfer* **40** (11), 2525–2537.

EKKAD, S. V., HUANG, Y. & HAN, J.-C. 1998 Detailed heat transfer distributions in two-pass square channels with rib turbulators and bleed holes. *Intl J. Heat Mass Transfer* **41** (23), 3781–3791.

FU, M. K., ARENAS, I., LEONARDI, S. & HULTMARK, M. 2017 Liquid-infused surfaces as a passive method of turbulent drag reduction. *J. Fluid Mech.* **824**, 688–700.

FUKAGATA, K., IWAMOTO, K. & KASAGI, N. 2002 Contribution of Reynolds stress distribution to the skin friction in wall-bounded flows. *Phys. Fluids* **14** (11), L73–L76.

FUKAGATA, K., KASAGI, N. & KOUMOUTSAKOS, P. 2006 A theoretical prediction of friction drag reduction in turbulent flow by superhydrophobic surfaces. *Phys. Fluids* **18** (5), 051703.

GARCÍA CARTAGENA, E. J., ARENAS, I., BERNARDINI, M. & LEONARDI, S. 2018 Dependence of the drag over super hydrophobic and liquid infused surfaces on the textured surface and Weber number. *Flow Turbul. Combust.* **100** (4), 945–960.

GARCÍA CARTAGENA, E. J., ARENAS, I., AN, J. & LEONARDI, S. 2019 Dependence of the drag over superhydrophobic and liquid infused surfaces on the asperities of the substrate. *Phys. Rev. Fluids* **4**, 114604.

GAVRILAKIS, S. 1992 Numerical simulation of low-Reynolds-number turbulent flow through a straight square duct. *J. Fluid Mech.* **244**, 101–129.

HAN, J. C., DUTTA, S. & EKKAD, S. 2000 *Gas Turbine Heat Transfer and Cooling Technology*. Taylor and Francis.

HAN, J. C. & ZHANG, Y. M. 1992 High performance heat transfer ducts with parallel broken and V-shaped broken ribs. *Intl J. Heat Mass Transfer* **35** (2), 513–523.

HAN, J. C., ZHANG, Y. M. & LEE, C. P. 1991 Augmented heat transfer in square channels with parallel, crossed, and V-shaped angled ribs. *Trans. ASME: J. Heat Transfer* **113**, 590–596.

HASEGAWA, Y. & KASAGI, N. 2011 Dissimilar control of momentum and heat transfer in a fully developed turbulent channel flow. *J. Fluid Mech.* **683**, 57–93.

HETSRONI, G., MOSYAK, A., ROZENBLIT, R. & YARIN, L. P. 1999 Thermal patterns on the smooth and rough walls in turbulent flows. *Intl J. Heat Mass Transfer* **42**, 3815–3829.

HUSSAIN, A. K. M. F. & REYNOLDS, W. C. 1970 The mechanics of an organized wave in turbulent shear flow. *J. Fluid Mech.* **41**, 241–258.

JUNG, T., CHOI, H. & KIM, J. 2016 Effects of the air layer of an idealized superhydrophobic surface on the slip length and skin-friction drag. *J. Fluid Mech.* **790**, R1.

KASAGI, N., HASEGAWA, Y., FUKAGATA, K. & IWAMOTO, K. 2012 Control of turbulent transport: less friction and more heat transfer. *Trans. ASME: J. Heat Transfer* **134** (3), 031009.

KESTIN, J. & RICHARDSON, P. D. 1963 Heat transfer across turbulent, incompressible boundary layers. *Intl J. Heat Mass Transfer* **6**, 147–189.

KIM, J. & MOIN, P. 1987 Transport of passive scalars in a turbulent channel flow. In *Turbulent Shear Flows* (ed. J.-C. André *et al.*), vol. 6, pp. 85–96. Springer.

KIRK, T. L., HODES, M. & PAPAGEORGIOU, D. T. 2017 Nusselt numbers for Poiseuille flow over isoflux parallel ridges accounting for meniscus curvature. *J. Fluid Mech.* **811**, 315–349.

KOMMINAHO, J., LUNDBLADH, A. & JOHANSSON, A. V. 1996 Very large structures in plane turbulent Couette flow. *J. Fluid Mech.* **320**, 259–285.

LAM, L. S., HODES, M. & ENRIGHT, R. 2015 Analysis of Galinstan-based microgap cooling enhancement using structured surfaces. *Trans. ASME: J. Heat Transfer* **137**, 091003.

LAUGA, E., BRENNER, M. P. & STONE, H. A. 2007 Microfluidics: the no-slip boundary condition. In *Handbook of Experimental Fluid Mechanics* (ed. C. Tropea, A. Yarin & J. F. Foss), pp. 1219–1240. Springer.

LEONARDI, S. & CASTRO, I. P. 2010 Channel flow over large cube roughness: a direct numerical simulation study. *J. Fluid Mech.* **651**, 519–539.

LEONARDI, S., ORLANDI, P., DJENIDI, L. & ANTONIA, R. A. 2004 Structure of turbulent channel flow with square bars on one wall. *Intl J. Heat Fluid Flow* **25**, 384–392.

LEONARDI, S., ORLANDI, P., DJENIDI, L. & ANTONIA, R. A. 2015 Heat transfer in a turbulent channel flow with square bars or circular rods on one wall. *J. Fluid Mech.* **776**, 512–530.

LEONARDI, S., ORLANDI, P., SMALLEY, R. J, DJENIDI, L. & ANTONIA, R. A. 2003 Direct numerical simulations of turbulent channel flow with transverse square bars on one wall. *J. Fluid Mech.* **491**, 229–238.

LINDEMANN, A. M. 1985 Turbulent Reynolds analogy factors for nonplanar surface microgeometries. *J. Spacecraft* **22** (5), 581–582.

LUCHINI, P., MANZO, F. & POZZI, A. 1991 Resistance of a grooved surface to parallel flow and cross-flow. *J. Fluid Mech.* **228**, 87–109.

LUNDBLADH, A. & JOHANSSON, A. V. 1991 Direct simulation of turbulent spots in plane Couette flow. *J. Fluid Mech.* **229**, 499–516.

MARTELL, M. B., PEROT, J. B. & ROTHSTEIN, J. P. 2009 Direct numerical simulations of turbulent flows over superhydrophobic surfaces. *J. Fluid Mech.* **620**, 31–41.

MAYNES, D. & CROCKETT, J. 2014 Apparent temperature jump and thermal transport in channels with streamwise rib and cavity featured superhydrophobic walls at constant heat flux. *Trans. ASME: J. Heat Transfer* **136**, 011701.

MAYNES, D., WEBB, B. W. & DAVIES, J. 2008 Thermal transport in a microchannel exhibiting ultrahydrophobic micro-ribs maintained at constant temperature. *Trans. ASME: J. Heat Transfer* **130**, 022402.

MAYNES, D., WEBB, B. W., CROCKETT, J. & SOLOVJOV, V. 2013 Analysis of laminar slip-flow thermal transport in microchannels with transverse rib and cavity structured superhydrophobic walls at constant heat flux. *Trans. ASME: J. Heat Transfer* **135**, 021701.

MIYAKE, Y., TSUJIMOTO, K. & NAKAJI, M. 2001 Direct numerical simulation of a rough-wall heat transfer in a turbulent channel flow. *Intl J. Heat Fluid Flow* **22**, 237–244.

NG, C.-O. & WANG, C. Y. 2014 Temperature jump coefficient for superhydrophobic surfaces. *Trans. ASME: J. Heat Transfer* **136**, 064501.

ORLANDI, P. 2000 *Fluid Flow Phenomena. A Numerical Toolkit*. Kluwer Academic.

ORLANDI, P., LEONARDI, S., TUZI, R. & ANTONIA, R. A. 2003 Direct numerical simulation of turbulent channel flow with wall velocity disturbances. *Phys. Fluids* **15** (12), 3587–3601.

ORLANDI, P. & LEONARDI, S. 2004 Passive scalar in a turbulent channel flow with wall velocity disturbances. *Flow Turbul. Combust.* **72**, 181–197.

ORLANDI, P. & LEONARDI, S. 2006 DNS of turbulent channel flows with two- and three-dimensional roughness. *J. Turbul.* **7**, N53.

ORLANDI, P., LEONARDI, S. & ANTONIA, R. A. 2008 Turbulent channel flow with either transverse or longitudinal roughness elements on one wall. *J. Fluid Mech.* **561**, 279–305.

ORLANDI, P. & PIROZZOLI, S. 2020*a* Turbulent flows in square ducts: physical insight and suggestion for turbulence modellers. *J. Turbul.* **21** (2), 106–128.

ORLANDI, P. & PIROZZOLI, S. 2020*b* Transitional and turbulent flows in rectangular ducts: budgets and projection in principal mean strain axes. *J. Turbul.* **21** (5–6), 286–310.

ORLANDI, P., SASSUN, D. & LEONARDI, S. 2016 DNS of conjugate heat transfer in presence of rough surfaces. *Intl J. Heat Mass Transfer* **100**, 250–266.

PARK, H., PARK, H. & KIM, J. 2013 A numerical study of the effects of superhydrophobic surface on skin-friction drag in turbulent channel flow. *Phys. Fluids* **25**, 110815.

PIROZZOLI, S., MODESTI, D., ORLANDI, P. & GRASSO, F. 2018 Turbulence and secondary motions in square ducts. *J. Fluid Mech.* **840**, 631–655.

PROMVONGE, P. & THIANPONG, C. 2008 Thermal performance assessment of turbulent channel flows over different shaped ribs. *Intl Commun. Heat Mass* **35**, 1327–1334.

RASTEGARI, A. & AKHAVAN, R. 2015 On the mechanism of turbulent drag reduction with super-hydrophobic surfaces. *J. Fluid Mech.* **773**, R4.

RASTEGARI, A. & AKHAVAN, R. 2018 The common mechanism of turbulent skin-friction drag reduction with superhydrophobic longitudinal microgrooves and riblets. *J. Fluid Mech.* **838**, 68–104.

REYNOLDS, O. 1961 On the extent and action of the heating surface of steam boilers. *Intl J. Heat Mass Transfer* **3**, 163–166 (reprinted from *Proc. Lit. Phil. Soc. Manchester*, 14 (5), pp. 7–12, 1874).

ROSENBERG, B. J., VAN BUREN, T., FU, M. K. & SMITS, A. J. 2016 Turbulent drag reduction over air-and liquid-impregnated surfaces. *Phys. Fluids* **28** (1), 015103.

ROSENGARTEN, G., STANLEY, C. & KWOK, F. 2007 Superinsulating heat transfer surfaces for microfluidic channels. In *Proceedings of the 18th International Symposium on Transport Phenomena, Daejeon, Korea*.

SEO, J. & MANI, A. 2016 On the scaling of the slip velocity in turbulent flows over superhydrophobic surfaces. *Phys. Fluids* **28** (2), 025110.

SETHIAN, J. A. & SMEREKA, P. 2003 Level set methods for fluid interfaces. *Annu. Rev. Fluid Mech.* **35** (1), 341–372.

SEWALL, E. A., TAFTI, K. D., GRAHAM, A. B. & THOLE, K. A. 2006 Experimental validation of large eddy simulations of flow and heat transfer in a stationary ribbed duct. *Intl J. Heat Fluid Flow* **27**, 243–258.

STALIO, E. & NOBILE, E. 2003 Direct numerical simulation of heat transfer over riblets. *Intl J. Heat Fluid Flow* **24**, 356–371.

TANDA, G. 2004 Heat transfer in rectangular channels with transverse and V-shaped broken ribs. *Intl J. Heat Mass Transfer* **47**, 229–243.

TACHIE, M. F., PAUL, S. S., AGELINCHAA, M. & SHAH, M. K. 2009 Structure of turbulent flow over 90° and 45° transverse ribs. *J. Turbul.* **10**, N20.

TEITEL, M. & ANTONIA, R. A. 1993 Heat transfer in fully developed turbulent channel flow: comparison between experiment and direct numerical simulations. *Intl J. Heat Mass Transfer* **36** (6), 1701–1706.

TILLMARK, N. & ALFREDSSON, P. H. 1992 Experiments on transition in plane Couette flow. *J. Fluid Mech.* **235**, 89–102.

VAN BUREN, T. & SMITS, A. J. 2017 Substantial drag reduction in turbulent flow using liquid-infused surfaces. *J. Fluid Mech.* **827**, 448–456.

VINUESA, R., NOORANI, A., LOZANO-DURÁN, A., EL KHOURY, G. K., SCHLATTER, P., FISCHER, P. F. & NAGIB, H. M. 2014 Aspect ratio effects in turbulent duct flows studied through direct numerical simulations. *J. Turbul.* **15** (10), 677–706.

WALSH, M. J. 1982 Turbulent boundary layer drag reduction using riblets. *AIAA Paper* 82-0169.

WALSH, M. J. 1983 Riblets as a viscous drag reduction technique. *AIAA J.* **21** (4), 485–486.

WEBB, R. L. 1981 Performance evaluation criteria for use of enhanced heat transfer surfaces in heat exchangers design. *Intl J. Heat Mass Transfer* **24** (4), 715–726.

WON, S. Y. & LIGRANI, P. M. 2004 Comparisons of flow structure and local Nusselt numbers in channels with parallel- and crossed-rib turbulators. *Intl J. Heat Mass Transfer* **47**, 1573–1586.